

University of Windsor

## Scholarship at UWindor

---

Electronic Theses and Dissertations

Theses, Dissertations, and Major Papers

---

7-29-2020

# Thermal Management of E–Motors in Electric Vehicle Application Employing LPTN Model

Muhammad Ali Ayub Towhidi  
*University of Windsor*

Follow this and additional works at: <https://scholar.uwindsor.ca/etd>

---

### Recommended Citation

Towhidi, Muhammad Ali Ayub, "Thermal Management of E–Motors in Electric Vehicle Application Employing LPTN Model" (2020). *Electronic Theses and Dissertations*. 8424.  
<https://scholar.uwindsor.ca/etd/8424>

This online database contains the full-text of PhD dissertations and Masters' theses of University of Windsor students from 1954 forward. These documents are made available for personal study and research purposes only, in accordance with the Canadian Copyright Act and the Creative Commons license—CC BY-NC-ND (Attribution, Non-Commercial, No Derivative Works). Under this license, works must always be attributed to the copyright holder (original author), cannot be used for any commercial purposes, and may not be altered. Any other use would require the permission of the copyright holder. Students may inquire about withdrawing their dissertation and/or thesis from this database. For additional inquiries, please contact the repository administrator via email ([scholarship@uwindsor.ca](mailto:scholarship@uwindsor.ca)) or by telephone at 519-253-3000ext. 3208.

**Thermal Management of E–Motors in Electric Vehicle Application  
Employing LPTN Model**

By

**Muhammad Ali Ayub Towhidi**

A Thesis  
Submitted to the Faculty of Graduate Studies  
through the Department of Electrical and Computer Engineering  
in Partial Fulfillment of the Requirements for  
the Degree of Master of Applied Science  
at the University of Windsor

Windsor, Ontario, Canada

2020

© 2020 Muhammad Ali Ayub Towhidi

**Thermal Management of E–Motors in Electric Vehicle Application Employing  
LPTN Model**

by

**Muhammad Ali Ayub Towhidi**

APPROVED BY:

---

O. Jianu  
Department of Mechanical, Automotive and Materials Engineering

---

B. Balasingam  
Department of Electrical and Computer Engineering

---

N. C. Kar, Advisor  
Department of Electrical and Computer Engineering

June 9, 2020

## **DECLARATION OF CO–AUTHORSHIP / PREVIOUS PUBLICATION**

### *I. Co–Authorship*

I hereby declare that this thesis incorporates material that is result of joint research as follows: Chapter 2 was co–authored with Pratik Roy, Firoz Ahmed, Alexandre Bourgault, Shruthi Mukundan and Aiswarya Balamurali under the supervision of Dr. Narayan C. Kar. My contributions were introduction, part of methodologies, analysis and discussion while the contributions by the co–authors were design overview, part of methodologies and review of the manuscript. Chapter 3 was co–authored with Firoz Ahmed, Shruthi Mukundan and Ze Li under the supervision of Dr. Narayan C. Kar. All the key ideas, primary contributions, experimental designs, data analysis, interpretation, and writing were performed by the author, and the contributions by the co–authors were electromagnetic simulation, experimentation and review of the manuscript. Chapter 4 was co–authored with Firoz Ahmed and Pratik Roy under the supervision of Dr. Narayan C. Kar. My contributions were computational fluid dynamic (CFD) theory and model development including results, analysis and discussion, while the contributions by the co–authors were the key ideas, heat transfer design, experimentation and review of the manuscript.

I am aware of the University of Windsor Senate Policy on Authorship and I certify that I have properly acknowledged the contribution of other researchers to my thesis, and have obtained written permission from each of the co–author(s) to include the above material(s) in my thesis. I certify that, with the above qualification, this thesis, and the research to which it refers, is the product of my own work.

### *II. Previous Publication*

This thesis includes 3 original papers that have been previously published/submitted for publication in peer reviewed journals, as follows:

Thesis Chapter	Publication title/full citation	Publication status*
Chapter 2	P. Roy, M. Towhidi, F. Ahmed, A. J. Bourgault, S. Mukundan, A. Balamurali, and N. C. Kar, “A Comprehensive Review of Thermal Design and Analysis of Traction Motors,” IEEE 28th International Symposium on Industrial Electronics, Vancouver, Canada, June. 2019.	Published
Chapter 3	M. Towhidi, F. Ahmed, S. Mukundan, Z. Li, and N. C. Kar, “Lumped Parameter Thermal Network Modeling for Online Temperature Prediction of Permanent Magnet Synchronous Motor for Different Drive Cycles in Electric Vehicle Applications,” SAE World Congress Experience Conference, Detroit, USA, April 2020.	Published
Chapter 4	F. Ahmed, P. Roy, M. Towhidi, G. Feng, and N. C. Kar, “CFD and LPTN Hybrid Technique to Determine Convection Coefficient in End-winding of TEFC Induction Motor with Copper Rotor,” IEEE 45th Annual Conference of the Industrial Electronics Society, Lisbon, Portugal, October 2019.	Published

I certify that I have obtained a written permission from the copyright owner(s) to include the above published material(s) in my thesis. I certify that the above material describes work completed during my registration as a graduate student at the University of Windsor.

### *III. General*

I declare that, to the best of my knowledge, my thesis does not infringe upon anyone’s copyright nor violate any proprietary rights and that any ideas, techniques, quotations, or any other material from the work of other people included in my thesis, published or otherwise, are fully acknowledged in accordance with the standard referencing practices. Furthermore, to the extent that I have included copyrighted material that surpasses the bounds of fair dealing within the meaning of the Canada Copyright Act, I certify that I have

obtained a written permission from the copyright owner(s) to include such material(s) in my thesis.

I declare that this is a true copy of my thesis, including any final revisions, as approved by my thesis committee and the Graduate Studies office, and that this thesis has not been submitted for a higher degree to any other University or Institution.

## ABSTRACT

The electric motor is at the center focus as an alternative to the internal combustion engine for automotive applications since it does not produce greenhouse gas emissions and can contribute significantly to the reduction of fossil fuel consumption globally. As extensive research works are being done on electric vehicles at present, thermal analysis of traction motor is increasingly becoming the key design factor to produce electric motors with high power and torque capabilities in order to satisfy electric vehicle driving requirements. Motor losses cause active heat generation in the motor components and excessive temperature rise affects the electromagnetic performance of the traction motor. High torque and power requirements based on the driving conditions under urban and highway drive conditions demand high capacity motor cooling system in order to keep the temperature within the safe limit. Hence, it is critical to develop and design a temperature prediction tool to dynamically estimate the winding and magnet temperature and regulate cooling to remove excessive heat from the motor. Conventional thermal modeling of motors includes analytical and numerical modeling. Analytical modeling is done by using Lumped Parameter Thermal Network (LPTN) which is analogous to electric circuit and a fast method for predicting temperature. It uses heat transfer equations involving thermal resistances and thermal capacitances to analytically determine temperature at different nodes. Numerical modeling is done in two ways—Finite Element Analysis and Computational Fluid Dynamics. Numerical modeling can produce more accurate results, but it requires more computational time. Since the temperature of motor components has to be predicted very quickly, i.e. during driving, LPTN is more effective because LPTN can quickly predict temperature based on the heat transfer equations. This thesis proposes an LPTN model that predicts motor temperature and regulates the required coolant flow rate simultaneously. Thus, it is able to dynamically predict the temperature. MATLAB Simulink has been used for simulation of the LPTN model for a laboratory PMSM prototype. The thermal resistances in the thermal network model have been obtained from the motor geometrical parameters. The electromagnetic loss data with respect to torque and speed were taken as input, and thus the temperature results of motor components have been found. The future work will be to implement this model into full scale prototype of the motor.

# **DEDICATION**

My Parents



## ACKNOWLEDGEMENTS

First of all, I would like to express my heartiest gratitude to Dr. Narayan C. Kar who always guided me throughout my Master's program. He was very helpful and conscious about my research progress since the very beginning. I received his valuable advices while studying, writing papers and presenting, and I must say I learnt a lot from him. I would never be able to finish my research and thesis in time without his continuous supervision and guidelines. I feel fortunate to have him as my supervisor. I appreciate all the support I got from him.

I am very grateful to Dr. Balakumar Balasingam and Dr. Ofelia A. Jianu for serving as my thesis committee members. They gave me their valuable suggestions to improve the technical content of my thesis. I thank them both very much.

I am very grateful to Dr. Firoz Ahmed who helped me to learn in-depth understanding of thermal designs of traction motors and guided me in every step. I am really thankful to Mr. Pratik Roy who was always there to help me in my research in every way. I would also like to thank Dr. Shruthi Mukundan, Dr. Himavarsha Dhulipati, Ms. Eunha Chu, and Mr. Ze Li for all their sincere cooperation throughout my MASc program. I am obliged to all my colleagues in the CHARGE labs as well.

## TABLE OF CONTENTS

<b>DECLARATION OF CO–AUTHORSHIP / PREVIOUS PUBLICATION .....</b>	<b>iii</b>
<b>ABSTRACT.....</b>	<b>vi</b>
<b>DEDICATION.....</b>	<b>vii</b>
<b>ACKNOWLEDGEMENTS .....</b>	<b>viii</b>
<b>LIST OF TABLES .....</b>	<b>xi</b>
<b>LIST OF FIGURES .....</b>	<b>xii</b>
<b>NOMENCLATURE.....</b>	<b>xv</b>
<b>CHAPTER 1: INTRODUCTION.....</b>	<b>1</b>
1.1. Overview .....	1
1.2. Objectives of the Thesis .....	3
1.3. Novelty and Contribution.....	6
1.4. Structure of the Thesis.....	7
References .....	8
<b>CHAPTER 2: A COMPREHENSIVE REVIEW OF THERMAL DESIGN AND ANALYSIS OF TRACTION MOTORS .....</b>	<b>10</b>
2.1. Introduction .....	10
2.2. Overview of Thermal Design and Analysis .....	12
2.2.1. Methodologies of Thermal Design and Analysis .....	12
2.2.2. Thermal Analysis of Active Cooling Design .....	14
2.2.3. Thermal Analysis of Passive Cooling Design .....	15
2.3. Design Overview of Traction Motors .....	16
2.4. Thermal Design of Traction Motors.....	17
2.4.1. Synchronous Motors.....	17
2.4.2. Induction Motors .....	18
2.5. Recommendations .....	19
2.5.1. Analytical Method .....	19
2.5.2. Numerical Method.....	20
2.6. Conclusion.....	20
References .....	21

<b>CHAPTER 3: LPTN MODELING FOR ONLINE TEMPERATURE PREDICTION OF PERMANENT MAGNET SYNCHRONOUS MOTOR FOR DIFFERENT DRIVE CYCLES IN ELECTRIC VEHICLE APPLICATIONS .....</b>	<b>28</b>
3.1. Introduction .....	28
3.2. Targeted Traction Motors and Drive Cycle Overview.....	29
3.3. Proposed Lumped Parameter Thermal Network (LPTN) Model.....	31
3.3.1. LPTN Model Overview .....	31
3.3.2. Analytical Solution of LPTN Model .....	32
3.3.3. Motor Loss Approximations for LPTN Model–Prototypes A and B .....	35
3.4. Heat Removal by Liquid Cooling .....	38
3.5. Experimental Setup for Thermal Tests.....	42
3.6. Results and Analysis .....	42
3.6.1. Simulations Results from the LPTN Model–IPMSM Prototype A.....	42
3.6.2. Simulations Results from the LPTN Model–IPMSM Prototype B .....	45
3.6.3. Experimental Validation of Temperature Results from LPTN Simulation .....	47
3.7. Conclusion.....	50
References .....	50
<b>CHAPTER 4: CFD AND LPTN HYBRID TECHNIQUE TO DETERMINE CONVECTION COEFFICIENT IN THE END–WINDING OF A TEFC INDUCTION MOTOR WITH COPPER ROTOR .....</b>	<b>53</b>
4.1. Introduction .....	53
4.2. Determination of Heat Transfer Coefficients.....	55
4.2.1. Natural Convection Coefficients from End–Winding.....	55
4.2.2. Determination of Air Flow Characteristics in the Stator End–Winding Region Using Computational Fluid Dynamic (CFD) Technique .....	59
4.3. Validation of Air Flow Characteristics in the End–Winding Region through Experiments.....	66
4.4. Conclusion.....	71
References .....	72
<b>CHAPTER 5: CONCLUSION AND FUTURE WORK .....</b>	<b>75</b>
5.1. Conclusion.....	75
5.2. Future Work .....	76
<b>APPENDIX .....</b>	<b>77</b>
<b>VITA AUCTORIS .....</b>	<b>81</b>

## LIST OF TABLES

Table 3.1. Technical Specifications of the IPMSMs .....	30
Table 3.2. Physical Parameters of the IPMSMs .....	30
Table 3.3. Selected Losses from Prototype A for UDDS and HWFET Conditions .....	37
Table 3.4. Selected Losses from Prototype B for UDDS Conditions.....	37
Table 4.1. Simplified Lumped Parameter Thermal Network Model .....	56
Table 4.2. Copper Rotor Induction Test Motor Data.....	58
Table 4.3. Key Physical Dimension Data of the Test Motor .....	58
Table 4.4. No Load Test Results for CRIM.....	58
Table 4.5. No Load Test Results for CRIM.....	59
Table 4.6. Boundary Conditions for 3D CFD Analysis.....	64
Table 4.7. Combined Natural and Forced Convection Heat Transfer Coefficients at Different Rotor RPM .....	69

## LIST OF FIGURES

Figure 1.1. Torque and power requirements of a traction motor .....	1
Figure 1.2. Torque–speed characteristics.....	1
Figure 1.3. Average motor life–hours with temperature.....	2
Figure 1.4. Demagnetization–NdFeB magnet [4].....	3
Figure 1.5. Heat transfer in electric motor [6] .....	4
Figure 1.6. FEA simulation of a motor [3].....	5
Figure 1.7. CFD simulation of a motor [3] .....	6
Figure 2.1. Simplified LPTN model of a traction motor [9].....	14
Figure 2.2. Temperature distribution of two different traction motors. (a) FEA results [10] and (b) CFD results [11]. .....	14
Figure 3.1. IPMSM prototype motors designed for EV. (a) Prototype A. (b) Prototype B. ....	30
Figure 3.2. Torque–speed graph for prototype A and prototype B.....	31
Figure 3.3. Proposed simplified Lumped Parameter Thermal Network.....	33
Figure 3.4. Simplified LPTN model in MATLAB Simulink to determine thermal characterization of the motor. ....	36
Figure 3.5. Major losses from the IPMSM prototype A for varying torque and speed conditions.....	36
Figure 3.6. Major losses from the IPMSM prototype B for varying torque and speed conditions.....	36
Figure 3.7. Experimental setup for thermal tests for prototype B .....	42
Figure 3.8. Stator winding temperature results from LPTN model for prototype A under 500 rpm and rated torque of 65 Nm condition.....	43
Figure 3.9. Temperature results from LPTN model for prototype A under 500 rpm and rated torque of 65 Nm condition. ....	43
Figure 3.10. Stator winding temperature results from LPTN model for prototype A under 2500 rpm and rated torque of 71 Nm condition.....	44

Figure 3.11. Stator winding temperature results from LPTN model for prototype A under 5000 rpm and rated torque of 50 Nm condition.....	44
Figure 3.12. Stator winding temperature results from LPTN model for prototype A under 500 rpm, 2500 rpm and 5000 rpm with 80% cooling.....	45
Figure 3.13. Stator winding temperature results from LPTN model for prototype A under 500 rpm, 2500 rpm and 5000 rpm with 90% cooling.....	45
Figure 3.14. Temperature results from LPTN model for prototype B under 300 rpm and rated torque of 65 Nm condition.....	46
Figure 3.15. Stator winding temperature results from LPTN model for prototype B under 300 rpm and rated torque of 65 Nm condition.....	46
Figure 3.16. Stator winding temperature results from LPTN model for prototype B under 600 rpm and rated torque of 65 Nm condition.....	46
Figure 3.17. Stator winding temperature results from LPTN model for prototype B under 1500 rpm and rated torque of 31 Nm condition.....	47
Figure 3.18. Winding temperature from experiments at 100 rpm for 40 Nm and 57 Nm torque.....	47
Figure 3.19. Winding temperature from experiments at 300 rpm for 49 Nm and 65 Nm torque.....	48
Figure 3.20. Comparison between experimental and simulation results at 100 rpm and 40 Nm.....	48
Figure 3.21. Comparison between experimental and simulation results at 100 rpm and 57 Nm.....	48
Figure 3.22. Comparison between experimental and simulation results at 300 rpm and 49 Nm.....	49
Figure 3.23. Comparison between experimental and simulation results at 300 rpm and 65 Nm.....	49
Figure 3.24. Magnet temperature at 44 and 58 Nm respectively at 100 rpm.....	49
Figure 3.25. Magnet temperature at 49 and 65 Nm respectively at 300 rpm.....	50
Figure 4.1. Published correlations for the equivalent heat-exchange coefficients in the end-regions for TEFC induction motors [3].....	54
Figure 4.2. A simplified lumped parameter model for end-winding.....	55
Figure 4.3. Measured temperatures for end-winding and inner air in the end-region.....	57

Figure 4.4. CRIM construction for the proposed study. ....	62
Figure 4.5. CFD models. (a) Smooth rotor end. (b) Small fin extensions. ....	62
Figure 4.6. Simplified geometry. (a) Isometric view. (b) Side view ....	63
Figure 4.7. Mesh created for stator end–winding CFD model. ....	63
Figure 4.8. Air flow pattern in the end–winding. (a) At rotor speed 200 r/min and without fin. (b) At rotor speed 1,200 r/min and without fin. (c) At rotor speed 200 r/min and with fin. (d) At rotor speed 1,200 r/min and with fin. ....	64
Figure 4.9. 3D CFD model simulated air velocity in the end–winding at 1,200 rpm (longitudinal section view). ....	65
Figure 4.10. 3D CFD model simulated air velocity in the end–winding at 1200 rpm (isometric view). ....	65
Figure 4.11. Experimental set–up for thermal tests on a 20hp CRIM. ....	66
Figure 4.12. Measured air velocity in the vertical axis to the end–winding plane. ....	67
Figure 4.13. Measured air velocity in the horizontal axis to the end–winding plane. ....	67
Figure 4.14. Combined convection coefficient with rotor peripheral speed (m/s). ....	70
Figure 4.15. Comparison of proposed correlation for convection coefficient with the published ones by other models. ....	70
Figure 4.16. Convection coefficient in the end–winding of the motor that has no fins on its end–rings. ....	71

## NOMENCLATURE

$R$	Thermal Resistance ( $^{\circ}\text{C}/\text{W}$ )
$L$	Axial length (m)
$K$	Thermal conductivity ( $\text{W}/\text{m}^{\circ}\text{C}$ )
$A$	Area of heat transfer ( $\text{m}^2$ )
$h$	Convection heat transfer coefficient ( $\text{W}/\text{m}^2^{\circ}\text{C}$ )
$T$	Temperature of a component ( $^{\circ}\text{C}$ )
$\varepsilon$	Emissivity
$\sigma$	Stefan–Boltzman constant ( $\text{W}/\text{m}^2^{\circ}\text{C}^4$ )
$F$	View factor
$Nu$	Nusselt number
$D_h$	Hydraulic diameter (m)
$f$	Friction factor
$Re$	Reynolds number
$Pr$	Prandtl number
$Gr$	Grashof number
$\omega$	Angular speed of rotor (rad/s)
$\rho$	Density of air ( $\text{kg}/\text{m}^3$ )
$\nu$	Kinematic viscosity of air ( $\text{m}^2/\text{s}$ )
$Ta$	Taylor number
$Ta_m$	Modified Taylor number
$F_g$	Geometric factor
$r_m$	Average radius of stator and rotor (m)
$\mu$	Dynamic viscosity of air ( $\text{Ns}/\text{m}^2$ )
$\theta$	Angle of each pole (rad)
$Q$	Rate of heat removal (W)
$m$	Mass flow rate of coolant (kg/s)
$C_p$	Specific heat of fluid ( $\text{J}/\text{kg}^{\circ}\text{C}$ )
$H$	Height of cooling channel (m)
$W$	Width of cooling channel (m)
$\Delta T$	Temperature difference between two nodes ( $^{\circ}\text{C}$ )



$\mathbf{U}$	Mean velocity vector (m/s)
$\mathbf{u}$	Velocity fluctuation vector (m/s)
$k$	turbulent kinetic energy ( $\text{m}^2/\text{s}^2$ )
$\varepsilon$	Rate of dissipation of turbulent kinetic energy ( $\text{m}^2/\text{s}^3$ )

# CHAPTER 1

## INTRODUCTION

### 1.1. Overview

Traction motors play an important role in electric vehicles because they provide the required propulsion power to the vehicle. The vehicle performance is highly dependent on the traction motor design and performance. That is why traction motor design must meet some operational requirements so that satisfactory vehicle performance can be ensured. For example, high torque is required at low speed for starting the vehicle or climbing up a hill or inclined gradient, and high power is necessary for maintaining high speed while cruising, as shown in Figure 1.1. High efficiency of the motor also has to be maintained over a wide range of torque and speed [1]. All these requirements cause significant heat generation in the motor, and as a result, the motor temperature increases.

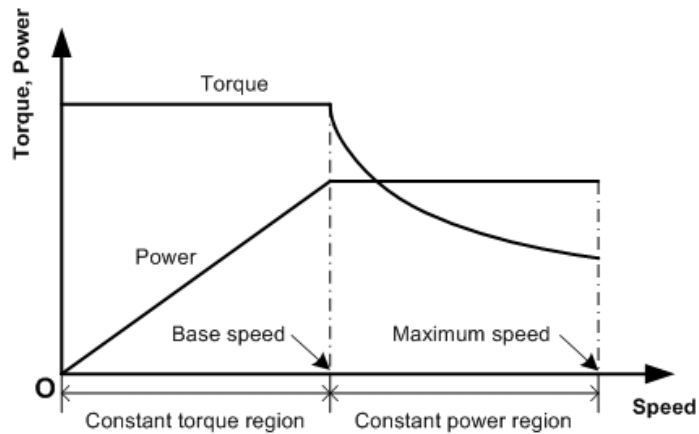


Figure 1.1. Torque and power requirements of a traction motor.

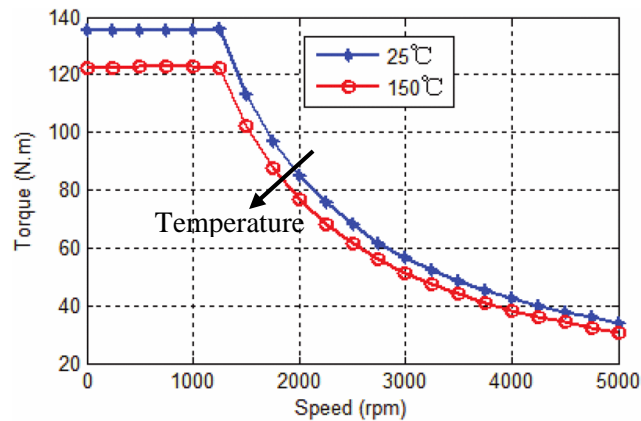


Figure 1.2. Torque-speed characteristics [2].

High temperature in the motor is not desirable as it can cause many issues. Firstly, the torque and power of the motor reduce significantly at high temperature, which indicates the effect of high temperature on motor performance. Ref. [2] showed a significant reduction of torque production by a motor at higher temperature. The authors found that the highest torque at zero speed reduces to 120 Nm at a temperature of 150°C, whereas it was 135 Nm at 25°C, as presented in Figure 1.2. It shows how the torque values reduce with increased temperature. Secondly, motor life decreases rapidly with high temperature. In general, motor life reduces by half because of a rise of temperature by 10°C. A comparison of life cycles of industrial motors with different insulation classes were analyzed for various operating temperatures in [3], which has been shown in Figure 1.3. Magnetic properties are also greatly affected by high temperature of the motor. This may lead to reduced electromagnetic performance of the motor and, in the case of permanent magnet motor, the motor may even be demagnetized completely and stop operating. For NdFeB magnet, the magnetizing intensity for zero magnetic flux was 1,200 kA/m at 20°C, which was reduced to 400 kA/m at a high temperature of 100°C [4] and is shown in Figure 1.4. Another problem is that the winding insulation material may be subject to breakdown if the temperature exceeds its melting point. Considering all these issues, it is very clear that motor temperature must be maintained within the safe operating limit. Therefore, there has to be a tool that can monitor the motor temperature and apply proper cooling so that the motor temperature remains within the safe limit.

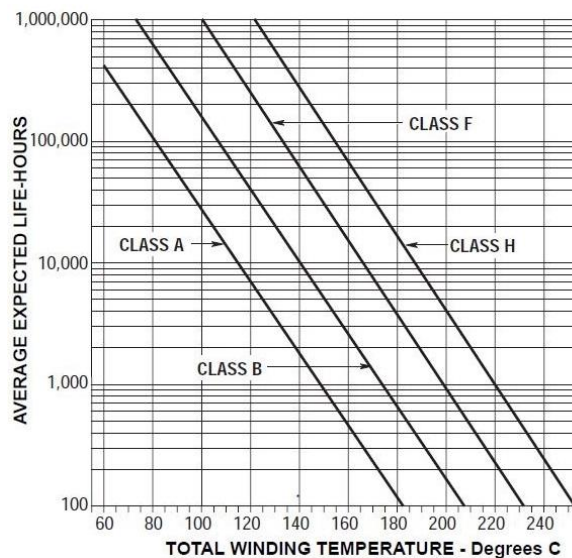


Figure 1.3. Average motor life–hours with temperature [3].

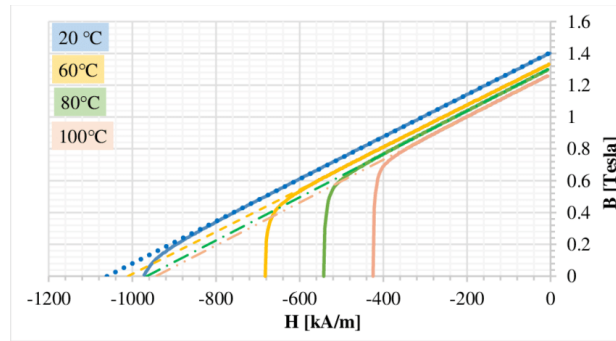


Figure 1.4. Demagnetization–NdFeB magnet [4].

There are three existing methods that are widely used to monitor motor temperature:

1. **Direct Measurement:** Resistance Temperature Detectors (RTDs) or thermocouples are used to directly measure the temperature of motor components. However, this is difficult to install in various motor components due to complex geometry of the motor. It also becomes expensive, especially in small and medium sized motors.
2. **Parameter–based Estimation:** Instead of directly measuring temperature, this technique measures resistance, which is considered as a function of temperature. Thus, the temperature is calculated based on the resistance value. However, this technique is very often subject to parametric errors, especially while the motor operates at high speed.
3. **Thermal Model–based Estimation:** This technique uses mathematical model, which addresses the overall heat transfer phenomenon. Since it only uses theoretical heat transfer equations, it is quite easy to implement. Thermal modeling is a very popular and effective way of motor temperature prediction. This technique has been used in this thesis to predict motor temperature

### ***1.2. Objectives of the Thesis***

Thermal modeling is the mathematical characterization of heat transfer phenomenon. Therefore, first the heat flow in a motor has to be determined in order to build a thermal model. Figure 1.5 shows a representation of all types of heat transfer associated with motor. At the very center of the motor, there is the shaft. Heat is generated in the rotor due to rotor core loss and magnet loss. A part of this heat goes to the shaft radially and along the shaft

axially, which is a conduction mode of heat transfer. Another part of the heat from rotor goes radially outward to the air-gap and axially to the enclosed free space, which is a convection heat transfer. Some portion of the heat from shaft also goes to the free space by convection heat transfer. A large amount of heat is generated in the stator because of stator winding loss and stator core loss. The heat in the stator core flows axially along the stator and radially to the outer casing. The heat in end-winding region goes to the enclosed air by convection and reaches the end-caps. Finally, the heat in the motor casing flows radially outward to the ambient by convection and radiation. Convection is the dominant mode of heat transfer there and radiation is negligible. A little portion of heat from the casing also goes axially along the casing to reach the end-caps and finally to the ambient by convection and radiation. Radiation is negligible in this case as well. Since the cooling channel has forced convection in it, the radiation resistance is much higher than convection resistance, and that is why the radiation heat transfer becomes negligible.

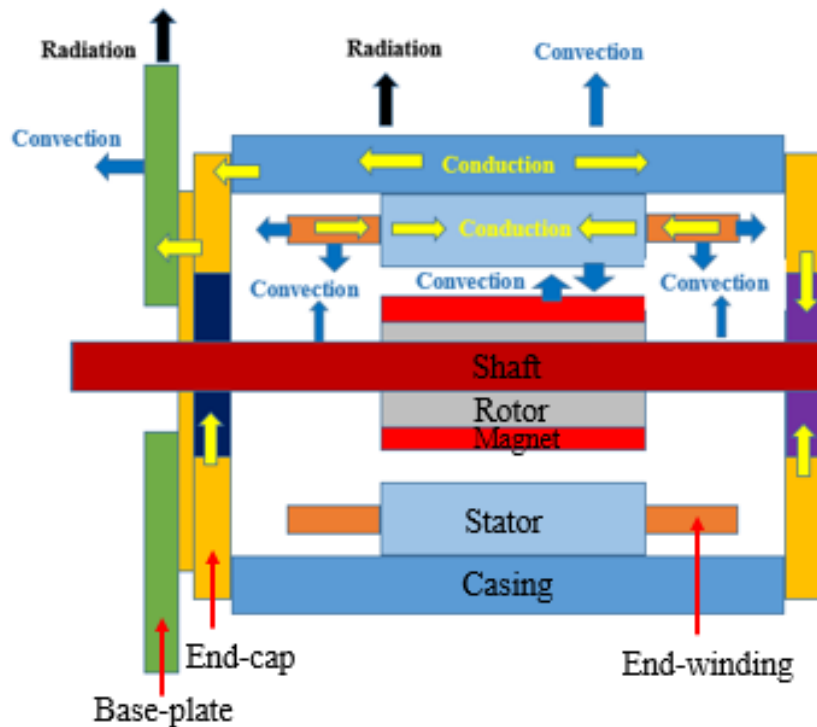
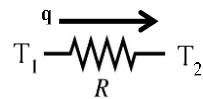


Figure 1.5. Heat transfer in electric motor [6].

There are two types of thermal models that can be used for traction motor thermal analysis.

### 1. Lumped Parameter Thermal Network (LPTN) Model:

LPTN model is a thermal model that represents the heat transfer phenomenon in terms of a network analogous to electric circuit. In electric circuit, current flows from one node to another due to the voltage difference between those two nodes. Similarly, in LPTN model, the heat flows from one node to another because of the temperature difference between the nodes. The current has to undergo a resistance while flowing from one node to another. Similarly, the heat has to face a thermal resistance while flowing between two nodes. Each component of a motor can be thought of as a node where the properties of the whole component is lumped. Heat flow is related to the temperature difference and thermal resistance in a similar way to Ohm's law. Thermal resistance can be found by using the heat transfer equations based on the type of heat transfer.



### 2. Numerical Model: Finite Element Analysis and Computational Fluid Dynamics:

Numerical models are the ones where differential equations are numerically solved in order to find the temperature. Finite Element Analysis uses conduction equation and considers thermal stress to model the temperature. Computational Fluid Dynamics solves Navier–Stokes equations and turbulence models to account for fluid flow characteristics and find the temperature results. An FEA result and a CFD result for traction motor have been shown in Figures 1.6 and 1.7, respectively.

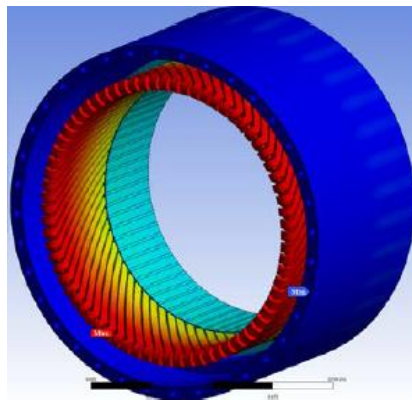


Figure 1.6. FEA simulation of a motor [3].

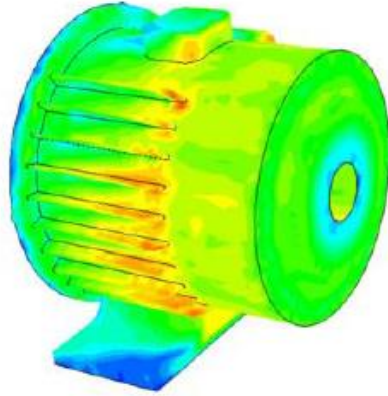


Figure 1.7. CFD simulation of a motor [3].

FEA has a longer computation time than LPTN, and CFD takes even much longer time than FEA. Since it is required to predict motor temperature quickly in dynamic condition, LPTN model is preferred in electric vehicle application. The next chapter discusses the comparison between the different types of thermal models and suggests how to implement them.

Since LPTN model is able to predict temperature quickly, which is required in electric vehicle application, the objectives of this thesis are:

1. To propose an LPTN model that predicts motor temperature for varying torque and power required by the EV motor.
2. To regulate required amount of cooling under different driving conditions.

It is very important to predict motor temperature during driving conditions so that the thermal health of the motor can be monitored instantaneously. Also, sufficient cooling must be provided to the motor in order to keep the motor thermally safe. While the motor is in operation, the quickest way to find the motor temperature is the use of LPTN model. That is why the objectives mentioned above have been chosen.

### ***1.3. Novelty and Contribution***

The existing LPTN models assume certain amounts of cooling applied to the motor but do not take the optimum flow rate into account. One of the nodes in the model is taken as the heat removal node, but it only assumes a certain amount of heat removal. Temperature

results depend on this heat removal amount, but the existing models do not have any established relationship to relate the heat removal rate with the liquid flow rate.

The LPTN proposed in this thesis in Chapter 3 has incorporated the liquid coolant flow rate in the LPTN model. Basic thermodynamic formula has been used first to equate the heat removed from motor and the heat absorbed by the liquid coolant. This is how the temperature is a function of mass flow rate of the coolant, and mass flow rate of the coolant is a function of the output temperature result. One of the key parameters in this relationship is the convection heat transfer coefficient, which is calculated from Nusselt number equations. Nusselt number is expressed as a function of Reynolds number, Prandtl number and friction factor. The equation for Nusselt number determination varies with the type of fluid flow and cooling channel geometry. Once the convection coefficient is obtained from the corresponding Nusselt number equation, the thermodynamic equilibrium is maintained by the variation of flow rate of the coolant. This flow rate variation has been implemented in the MATLAB Simulink model.

Incorporating the required coolant flow rate in the LPTN model ensures that only the required amount of cooling liquid flows through the channel. So, the energy required to run the coolant flow cycle will be properly utilized and will not be wasted. At the same time, enough cooling effect ensures the motor to be within safe limit of temperature by means of forced convection in the cooling channels. The safe limits of temperature for the motors used in this thesis are 110°C and 120°C, respectively.

#### ***1.4. Structure of the Thesis***

A comprehensive review of thermal analysis and design techniques for traction motors has been done in Chapter 2 of this thesis. Thermal modeling for Permanent Magnet Synchronous Motors and Induction Motors have been studied and compared. Analytical method and numerical method of thermal modeling have been discussed and compared for each type of traction motors. Active cooling and passive cooling have also been discussed for both types of traction motor. Finally, some recommendations are provided about how LPTN and numerical methods can be implemented in thermal study of different types of traction motors in order to get satisfactory results.



An LPTN model has been proposed in Chapter 3 for online temperature prediction of Permanent Magnet Synchronous Motors in electric vehicle application. Both UDDS and HWFET drive cycles have been considered for two PMSM prototypes in the CHARGE labs. Thermal resistances and capacitances in the LPTN model have been found from the geometrical parameters of the motor prototypes. A relationship between the flowrate of cooling liquid and motor temperature has been established and implemented in the LPTN cooling blocks in MATLAB Simulink. Taking loss data of the motors with respect to torque and speed as input, the LPTN model simulation has given temperature results of motor components as output. A few experimental results have been found for one of the prototypes.

A CFD and LPTN hybrid technique has been proposed for determining the convection coefficient in the end-winding region of induction motor with copper rotor. A thermal network has been built for the end-winding region, and the thermal resistances have been determined from natural convection condition. The air flow behavior in the end-winding region has been characterized by RANS equations with  $k-\epsilon$  model. The air flow velocity results in the end-winding region have been used to determine the forced convection coefficient from empirical relationships of Grashof number, Prandtl number, Reynolds number and Nusselt number. The convection coefficient has been related to the rotor speed by means of an equation which can be used for different sizes of induction motors with copper rotor.

The research findings of the chapters have been mentioned in Chapter 5. The next probable research steps have been recommended as the future work.

### ***References***

- [1] L. V. Iyer, "Investigation of permanent magnet synchronous machines for direct-drive and integrated charging applications in electric vehicles," Ph.D. Dissertation, University of Windsor, 2016.
- [2] Z. Zhang *et al.*, "Research on effect of temperature on performance and temperature compensation of interior permanent magnet motor," *IEEE 11th Conference on Industrial Electronics and Applications (ICIEA)*, June 2016.

- [3] J. Pierre–Oliver and L. Jean, “Heat transfer in electric machines,” presented in a webinar by EOMYS Engineering, September 2017.
- [4] F. János *et al.*, “Experimental investigation of the temperature dependence of the air–gap flux density in a permanent magnet synchronous machine,” *XXXIV Kando Konferencia Science in Practice*, Hungary, November 2018.
- [5] B. Venkataraman, B. Godsey *et al.*, “Fundamentals of a motor thermal model and its applications in motor protection,” *Annual Conference for Protective Relay Engineers*, 2005.
- [6] G. Demetriades, H. Parra, E. Andersson, and H. Olsson, “A real–time thermal model of a permanent magnet synchronous motor based on geometrical measures,” *IEEE Power Electronics Specialists Conference*, 2008.
- [7] J. Holman, *Heat Transfer*. 9th ed., McGraw–Hill, 2002, pp. 640–647.

## **CHAPTER 2**

### **A COMPREHENSIVE REVIEW OF THERMAL DESIGN AND ANALYSIS OF TRACTION MOTORS**

#### ***2.1. Introduction***

Nowadays due to zero CO<sub>2</sub> emission, electric vehicles are gaining significant thrust from governments and automobile manufacturers globally to address environmental concern. Furthermore, rising fossil-fuel cost and recent imposed tax on fossil-fuel in several developed countries are greatly influencing the shifting of research trends towards electric vehicles from fossil-fuel dependent vehicles. As the higher price of electric vehicles can be compensated by comparatively lower operational costs i.e. fuel and maintenance cost in the long run, more focus has been given to increase both speed and distance range of electric vehicles to make these environment friendly vehicles a more consumer friendly choice. This effort mostly depends on traction motors, which provide power to hybrid electric vehicles partially or full electric vehicles solely. Therefore, traction motors are receiving more and more attention in the research area of electric motor design.

In the past, most of the design and analysis of electric motors typically included the consideration and calculation of electromagnetic parameters. But during operation, most of the amount of energy losses in traction motors are converted into heat energy, which negatively affects the motor's performance. As a result, the more the losses, the more the temperature rise but the less the output power and the less the efficiency. Moreover, resistance of conductors increases with the increase in temperature leading to additional losses. Further, electromagnetic properties of core materials are also dependent on temperature and hence, electromagnetic performance of motors can also be affected, if the temperature goes beyond a permissible limit. In addition, a good percentage of motor failures are caused by overheating while in operation [1]. On the other hand, to meet the future demand for more consumer-friendly electric vehicle, high power density motor is needed along with considerable reduction in size. However, thermal stability for such compact size and high-power density motor is extremely poor especially without proper and improved thermal design. Therefore, recently, thermal design improvement for traction motors is getting more attention by researchers around the world.

In order to analyze the thermal aspects of traction motors, most of the researchers follow different basic methods that already exist which can generally be divided into analytical and numerical methods. Analytical method includes Lumped Parameter Thermal Network (LPTN) modeling where the thermal system is represented as a network of thermal resistances. Unlike LPTN modeling, numerical method considers the geometry of the overall system and calculates the heat transfer parameters. Depending on implementation of thermodynamics or fluid dynamics equations, numerical method can further be divided into Finite Element Analysis (FEA) and Computational Fluid Dynamics (CFD), respectively. But unlike typical thermal design and analysis, the simplified geometry and material properties generally used in machine design and construction are not sufficient to give an accurate prediction of the thermal performance of traction motors. Some critical parameters such as interference gaps between components, heat transfer across the air gap, uncertainty of material property, bearing and end–shield models etc. must be implemented into the basic thermal design and analysis. At the moment, there is abundant literature focusing on the implementation of different critical parameters of traction motors into thermal design. In most cases, research papers are focused on specific thermal design and analysis in a specific motor due to different types of complexities that come up with the changes in structure, characteristics and types of motor used. However, no guideline for selection or implementation of a suitable method for thermal design and analysis of traction motors exists. Therefore, this chapter primarily focuses on review of several methodologies of thermal design that have already been implemented in various types of traction motors. Finally, this chapter will identify and compare the strengths and weaknesses of those methodologies for thermal design and further develop a set of recommendations for improved and efficient ways to carry out those methods.

At present, two types of traction motors are mainly used in electric vehicles—synchronous motor and induction motor. Among synchronous motors, permanent magnet synchronous motor (PMSM) is mostly used in automotive sector due to its high efficiency and reduced size. PMSM has a unique construction where permanent magnets are placed in the rotor to create a constant magnetic field. Therefore, an additional node for permanent magnet associated with magnet loss is considered in LPTN modeling of PMSM [22]–[30]. Similarly, in numerical methods, magnet loss is also considered during thermal analysis of

PMSM [31]–[38]. PMSM is divided into two categories according to their rotor construction. One is rotor with surface mounted permanent magnets called surface mounted PMSM and another one is rotor with embedded permanent magnets called interior PMSM. According to their construction geometry, thermal designs of both surface mounted [6] and interior [12] PMSMs are carried out differently. Although other synchronous motors are rarely used in electric vehicles, there are still some papers on thermal analysis of switch reluctance motor [39] and electrically excited synchronous motor [40] where thermal design has been done by following the structural and electromagnetic design of each motor type using both analytical and numerical methods.

Besides synchronous motors, induction motors are also used as traction motors because of low maintenance, low cost and ability to operate even in hostile conditions. Unlike PMSM, induction motors do not have any permanent magnet, but have rotor bars which must be taken into consideration during thermal design and analysis. There are several papers on both analytical LPTN method [41]–[50] and numerical methods [49]–[61] for thermal design of induction motors.

## **2.2. Overview of Thermal Design and Analysis**

### *2.2.1. Methodologies of Thermal Design and Analysis*

Analytical LPTN model is mainly a thermal circuit consisting of several thermal resistances and capacitances, which accurately models the nature and path of the heat transfer. It is done by calculating thermal resistances based on conduction, convection and radiation heat transfer processes using (2.1), (2.2) and (2.3) respectively [2], [3].

$$R_{cond} = L/kA \quad (2.1)$$

$$R_{conv} = 1/hA \quad (2.2)$$

$$R_{rad} = (T_1 - T_0)/(\sigma\varepsilon F(T_1^4 - T_0^4)A) \quad (2.3)$$

where,  $R$  is the thermal resistance,  $L$  is the length,  $k$  is the thermal conductivity,  $A$  is the area,  $h$  is the convection heat transfer coefficient,  $T$  is the temperature,  $F$  is the view factor,  $\varepsilon$  is the emissivity and  $\sigma$  is the Stefan–Boltzmann constant.

Due to the ease and simplicity of modeling, LPTN has been implemented for thermal design and analysis of traction motors in numerous papers. As it is analogous to electric circuit network, it is a well adopted method in traction motors. LPTN model generally consists of several temperature nodes, which represent different motor components as lumped heat capacity elements where temperature is considered to be uniform. LPTN model must be detailed enough to cover all major motor components such as stator yoke, stator teeth, rotor, winding etc. which have bulk thermal storages and heat generation sources due to internal energy and losses [4]. Finally, thermal resistances and capacitances in those motor components are calculated and incorporated into transient or steady state thermal model equations to determine the nodal temperature rise.

Several references have also used numerical methods i.e. FEA and CFD for thermal design and analysis of traction motors. Both numerical methods have higher accuracy but are time consuming. Both methods are usually carried out by different industry standard software tools in which useful equations and processes are already integrated.

In FEA, losses are converted into heat sources and later on, temperature rise associated with heat sources is determined based on transient or steady state thermal condition [3]. Since only a very small portion of losses convert into sound and other forms of energy, temperature predicted by FEA is more accurate. Temperature rise was found almost identical with test results in [5]. Still slight temperature difference with test results can be found because it is difficult to design an identical 3D geometry for analysis. The most challenging part is to design the windings. Equivalent winding geometry is usually designed to simplify the process. As a result, it is difficult to achieve exact winding temperature in FEA [6]. Performing FEA at different loading conditions also contributes to the error [7].

Further, when a fluid flow is involved, it is better to use CFD to predict more realistic results. Unlike FEA, fluid dynamics equations integrated into CFD help to analyze the changes in fluid flow effectively. Moreover, boundary conditions, types and patterns of flow are well addressed by the integrated physics options available. CFD is also performed in equivalent geometry to simplify the process which contributes to the error [8].

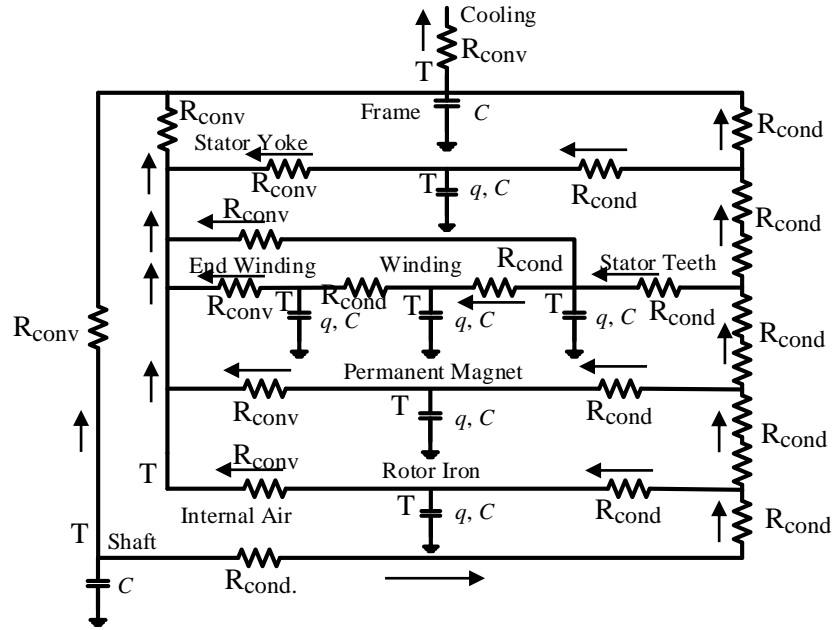


Figure 2.1. Simplified LPTN model of a traction motor [9].

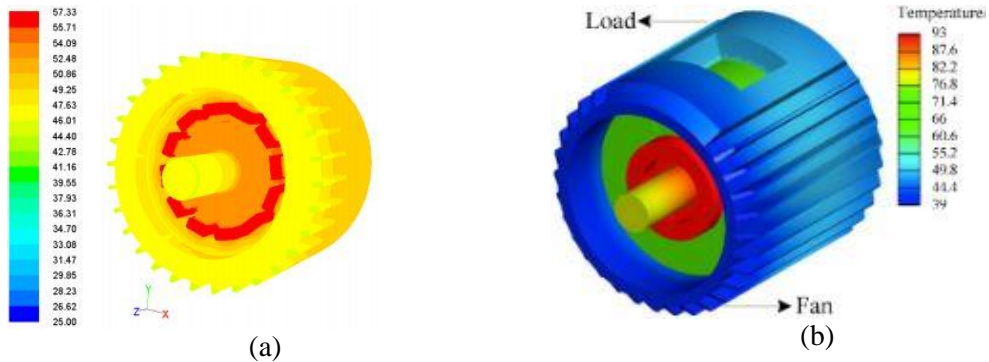


Figure 2.2. Temperature distribution of two different traction motors. (a) FEA results [10]. (b) CFD results [11].

### 2.2.2. Thermal Analysis of Active Cooling Design

Active cooling system in the form of forced air cooling, water or water–glycol cooling, oil cooling etc. is one of the integrated parts of traction motors to extract the generated heat from the motor and keep it thermally stable during operation. Therefore, active cooling system needs to be incorporated in thermal design to predict the temperature correctly. In LPTN method, there are some analytical approaches available to address active cooling effect. As convection is the primary heat transfer phenomenon in the cooling system, the convection heat transfer coefficient between cooling fluid and contact surface is being calculated for determining the thermal resistance for convection. The most common

approach for calculating the convection heat transfer coefficient is using (2.4) which involves Nusselt number [6], [9].

$$Nu = hD_h / k_f = \frac{(f/8)(Re-1000)Pr}{1 + 12.7(f/8)^{1/2}(Pr^{2/3}-1)} \quad (2.4)$$

where,  $k_f$  is the thermal conductivity of fluid,  $Nu$  is the Nusselt number,  $Re$  is the Reynolds number,  $Pr$  is the Prandtl number,  $D_h$  is the hydraulic diameter and  $f$  is the friction factor.

According to the flow pattern, turbulence intensity and cooling techniques, some of the papers have also suggested several alternative equations to determine Nusselt number [12]–[14]. These strategies are applied in LPTN for all types of cooling according to the conditions except for air cooling. During forced air cooling, which is mainly used in induction motors by means of fans or blowers, a validated equation is used for convection heat transfer coefficient [15]–[17] as,

$$h = k_1 \times [1 + (k_2 v)^{k_3}] \quad (2.5)$$

where,  $h$  is convection heat transfer coefficient dependent on inner air velocity  $v$  in the end region,  $k_1$ ,  $k_2$  and  $k_3$  are proportionality constants dependent on air turbulence in the end region.

In case of numerical methods, CFD is the best way for thermal analysis of active cooling system of traction motors, as fluid flow is involved. In CFD, turbulence modeling of cooling fluid is done using different approaches such as standard  $k-\epsilon$ , realizable  $k-\epsilon$ , standard  $k-\omega$  etc. based on applications to determine the convection heat transfer coefficient [14], [18].

### 2.2.3. Thermal Analysis of Passive Cooling Design

When any active cooling is not present in the motor, there is always certain amount of natural air flow within the end-space between the rotor and the end-cap, which is responsible for natural passive cooling. Because of compact construction of traction motors, it is challenging to address natural passive cooling. Equations (2.6) and (2.7) have been considered to determine the convection heat transfer coefficient of natural air flow due to both laminar and turbulent nature of the air flow within the end-space [19].



$$\left. \begin{aligned} h_t &= 0.35k_{air}\left(\frac{\omega}{v}\right)^{0.5}; \text{Re} < 30,000 \\ &= 0.0195\frac{k_{air}}{r_{ro}}\left(\frac{\omega r_{ro}^2}{v}\right)^{0.8}; \text{Re} \geq 30,000 \end{aligned} \right\} \quad (2.6)$$

$$h_l = \frac{0.59(Gr Pr)^{0.25}}{R_{ec}} \quad (2.7)$$

where,  $h_t$  and  $h_l$  are the coefficients of air convection within the end-space near the rotor and the end-cap respectively,  $k_{air}$  is the thermal conductivity of air,  $\omega$  is the angular velocity of rotor,  $r_{ro}$  is the outer radius of rotor core and  $R_{ec}$  is the end-cap axial thermal resistance.

There are also several other approaches available to calculate that natural convection coefficient. In case of induction motor, (2.5) can be used for calculation of the natural convection coefficient [16]. Although these analytical approaches are common methods, CFD analysis is the better way for calculation of the natural convection coefficient similar to active cooling.

In some cases, fins are normally placed on the surface of motor housing to improve the natural air cooling effect. To incorporate cooling effects of fins, in LPTN modeling, thermal resistances due to all three types of heat transfer processes are determined in fins section [15], [16] and in numerical methods, geometry and material properties of fins are considered.

### **2.3. Design Overview of Traction Motors**

Accuracy of thermal design and analysis of traction motors mostly depends on electromagnetic and structural design of the motors. Therefore, the changes in electromagnetic and structural design due to the change in motor type must be addressed during thermal design. This is done by considering all major motor components and all losses in those components such as core loss, copper loss, friction loss etc. To address electromagnetic losses, thermal analysis is always coupled with electromagnetic analysis, which is carried out through analytical approach [20] or electromagnetic FEA [21]. Other losses, which are generally regarded as mechanical losses, such as bearing losses can be calculated from manufacturer's manual.

## ***2.4. Thermal Design of Traction Motors***

In this section, strengths and weaknesses of some of the implemented thermal designs are identified for both synchronous and induction motors.

### *2.4.1. Synchronous Motors*

In [27], a simplified LPTN model consisting of ten nodes was designed for water cooled interior PMSM. Combination of conduction and convection expressions was used for water cooling system in the LPTN modeling. Temperature difference with FEA results was found to be between 1–6°C. However, absence of thermal capacitances made it impossible to analyze transient thermal state and also there was no calculation done for natural air cooling. Absence of thermal capacitances was also noticed in the LPTN model of water-cooled PMSM proposed in [19]. However, this LPTN model included more than ten nodes, which can address temperatures of different parts of the motors briefly at steady state. It addressed the effect of both active and passive cooling on the motor. For natural passive air cooling, method of two series thermal resistances was adopted using (2.6) and (2.7) due to laminar nature of air flow near the end-cap and turbulent nature of air flow near the high speed rotational rotor. A temperature difference of about 1–4°C from experimental results was observed. In [9], [24] and [26], the established LPTN models of PMSM had capacitances which enabled those LPTN models to analyze transient thermal state. In [24], there was a significant temperature difference up to 15°C between LPTN and experimental results, because of empirical loss modeling approach instead of finite element loss model approach. For this reason, to improve estimation accuracy, particle swarm optimization is applied for strategic fitting of uncertain parameters. After that improvement, a maximum temperature difference of 8°C was found, which can still be reduced further. On the contrary, in [26], finite element model approach was adopted for loss calculations. This LPTN model included equivalent rectangular shape transformation approach for stator slot geometry to simplify the calculation. Yet, the temperature difference with the experimental results was small, 4°C corresponds to an error of approximately 11%. One limitation of the LPTN model was considering the heat transfers in radial direction only. This limitation was later addressed in [9] and got quite convincing comparative graph with experimental results. In this paper, loss distribution was adjusted under consideration of driving duty cycle to enable LPTN model to predict dynamic temperature distribution.

In [5], thermal analysis of PMSM was carried out through FEA and compared with experimental results. It showed identical results up to 40 minutes and after that less than 10°C difference was found in winding temperature. In [6], reasons of errors in FEA results were observed due to mismatch in complicated geometry of distributed windings and uncertain data of anisotropic materials. An equivalent winding model was adopted and some assumptions were considered to deal with both situations in a simplified way. Still the accuracy of FEA results was better compared to LPTN results. The temperature difference between two results was 5.1°C in end winding. On the other hand, in [14], [18], [33], and [34], CFD was implemented, as these papers were mainly focused on cooling design for the motors. In [33] and [34], the shear–stress transport (SST)  $k-\omega$  model was used for turbulence modeling specifically, as this is more reliable for a wider class of fluid flows. In [14] and [18], all other approaches for turbulence modeling were also described briefly including the shear–stress transport (SST)  $k-\omega$  model. It was concluded that Reynolds stress transport (RST) and  $k-\epsilon$  model were suitable for turbulent core flows away from walls and  $k-\omega$  models were suitable near boundary layer flows. Moreover, these two papers also showed dependency of CFD results on the quality of data input such as mesh size, boundary conditions etc. besides turbulence modeling. Another challenge with implementing CFD is designing the equivalent geometry of windings, which was addressed in [8]. A well–designed equivalent geometry simplified the process as well as gave almost accurate results with only 1.5°C error in the paper.

#### *2.4.2. Induction Motors*

In [42], a low order simplified LPTN model was proposed through a reduced number of motor elements for induction motor and the maximum discrepancy with experimental results was found to be  $\pm 5^\circ\text{C}$ . On the other hand, in [16], a higher order LPTN model consisting of more than ten nodes was proposed for a fan cooled induction motor considering most of the motor components and heat transfer paths. The difference between predicted and experimental results was only 2–3°C. Fins were addressed and Schubert’s model modified version of (2.5) was used to calculate both natural and forced air cooling effects in this model. Due to complexity in determining exact value of inner air speed, the rotor peripheral speed was used for estimation. Radiation was neglected in both models. In [45], significant effect of radiation on motor temperature was observed during

determination of radiation thermal resistances in an induction motor at very low speed or in absence of motor fan. Therefore, radiation should be taken into account for accuracy of LPTN results at very low speed or during absence of motor fan. Moreover, there were some unique approaches such as general arc–segment element [62] and cuboidal element [63] for three–dimensional thermal modeling in analytical method to address material’s anisotropy for more accuracy.

In [52], a new approach for numerical method was adopted for thermal analysis of induction motor through a coupled FEA and CFD analysis. In this way, convection heat transfer coefficients can be determined more accurately by CFD and then using that coefficient into FEA, temperature distribution of the whole motor can be presented in less time compared to CFD analysis. Final temperature range of motor was 123–136°C, which was quite convincing compared to experimental result.

## ***2.5. Recommendations***

In this section, some recommendations are put forward regarding the efficient way of carrying out both analytical and numerical thermal design methods. Further, the efficient way of addressing cooling effects in those methods are also suggested.

### *2.5.1. Analytical Method*

In analytical method, the best way to design LPTN model is considering all the basic motor components and addressing all the significant heat transfer paths in both axial and radial directions. Also, both active and passive cooling effects must be included in the model by addressing both conduction and convection heat transfer, which occur during cooling. To address convection in an efficient way, Nusselt number equation must be chosen carefully based on flow pattern such as laminar or turbulent flow and cooling techniques, such as finned housing, housing jacket or spray cooling etc. to determine accurate convection heat transfer coefficient. Furthermore, if flow is turbulent, turbulence intensity must be taken into consideration also. Besides thermal resistances, LPTN model must consist of thermal capacitances also for transient thermal analysis. In addition, all losses must be taken into consideration to calculate temperature rise. Electromagnetic losses must be calculated accurately by finite element model analysis which enables consideration of loss coefficient varying with frequency and flux density instead of

constant loss coefficient. Other losses can be calculated from manufacturer's manual. Further, loss distribution must be taken into account under the driving duty cycle to predict dynamic temperature distribution throughout the motor.

### *2.5.2. Numerical Method*

In case of numerical methods, the best way is using coupled FEA and CFD where CFD addresses the changes in convection coefficient of cooling system which is used to estimate the temperature distribution using FEA to reduce the overall operation time for the whole process. The accuracy of such a process is primarily dependent on accurate calculation of losses and turbulence modeling of CFD. The losses should be addressed in a way similar to LPTN modeling and turbulence modeling approach must be chosen carefully based on the application. Thereby, more accurate results can be obtained as CFD addresses the small changes in convection coefficient effectively by simulating 3-D fluid flow with a higher degree accuracy, which cannot be done using empirical equations. Similarly, for more accuracy in LPTN, it can also be coupled with CFD in the same way. Further, while implementing numerical methods, equivalent model approach can be adopted for complex geometry of windings, which will simplify the process and reduce the operation time. Effective equivalent geometry has negligible effects on the final results.

## **2.6. Conclusion**

From literature, methodologies of thermal design and analysis incorporating the effects of electromagnetic characteristics, construction geometry and cooling design of traction motors have been described thoroughly. Some strengths and weaknesses of those proposed thermal designs have been pointed out. Further, some recommendations have been provided from the overall review for future references to design thermal model of any traction motor in a simplified way by addressing all those changing factors effectively with the change in type of traction motor used. Finally, such guidelines will be helpful for simplifying the process to avoid over-complexity and reduce operation time, while effective implementation strategy for all those important factors will ensure accuracy.

## References

- [1] G. Liao and J. Xi, "Intelligent monitoring and overheating protection system for motor," *International Conference on Computing, Control and Industrial Engineering*, Wuhan, 2010, pp. 308–311.
- [2] S. Ramarathnam, A. K. Mohammed, B. Bilgin, A. Sathyan, H. Dadkhah, and A. Emadi, "A review of structural and thermal analysis of traction motors," *IEEE Transactions on Transportation Electrification*, vol. 1, no. 3, pp. 255–265, Oct. 2015.
- [3] H. Li and Y. Shen, "Thermal analysis of the permanent-magnet spherical motor," *IEEE Transactions on Energy Conversion*, vol. 30, no. 3, pp. 991–998, Sept. 2015.
- [4] P. H. Mellor, D. Roberts, and D. R. Turner, "Lumped parameter thermal model for electrical machines of TEFC design," in *IEEE Proceedings B–Electric Power Applications*, vol. 138, no. 5, pp. 205–218, Sept. 1991.
- [5] L. Li, J. Zhang, C. Zhang, and J. Yu, "Research on electromagnetic and thermal issue of high-efficiency and high-power-density outer-rotor motor," in *IEEE Transactions on Applied Superconductivity*, vol. 26, no. 4, pp. 1–5, June 2016.
- [6] F. JinXin, Z. ChengNing, W. ZhiFu, and E. G. Strangas, "Thermal analysis of water cooled surface mount permanent magnet electric motor for electric vehicle," *International Conference on Electrical Machines and Systems*, Incheon, 2010, pp. 1024–1028.
- [7] A. Nollau and D. Gerling, "A new cooling approach for traction motors in hybrid drives," *International Electric Machines & Drives Conference*, Chicago, IL, 2013, pp. 456–461.
- [8] W. Zhao, L. Chen, G. Lin, and J. Ji, "Computational fluid dynamics thermal prediction of fault tolerant permanent-magnet motor using a simplified equivalent model," in *Progress in Electromagnetic Research M*, vol. 42, pp. 199–209, 2015.
- [9] J. Fan *et al.*, "Thermal analysis of permanent magnet motor for the electric vehicle application considering driving duty cycle," in *IEEE Transactions on Magnetics*, vol. 46, no. 6, pp. 2493–2496, June 2010.
- [10] J. Kuria and P. Hwang, "Investigation of thermal performance of electric vehicle BLDC motor," in *International Journal of Mechanical Engineering*, vol. 1, no. 1, Mar. 2012.

- [11] Y. Xie, J. Guo, P. Chen, and Z. Li, “Coupled fluid thermal–analysis for induction motors with broken bars operating under the rated load” in *Energies*, vol. 11, no. 8, pp. 2024, Aug. 2018.
- [12] X. Fan, B. Zhang, R. Qu, J. Li, D. Li, and Y. Huo, “Comparative thermal analysis of IPMSMs with integral–slot distributed–winding (ISDW) and fractional–slot concentrated–winding (FSCW) for electric vehicle application,” *IEEE International Electric Machines and Drives Conference (IEMDC)*, Miami, FL, 2017, pp. 1–8.
- [13] X. Zhang, Q. Lu, Y. Zhang, X. Huang, and Y. Ye, “Thermal characteristics study of a water–cooled permanent magnet linear motor,” *Ninth International Conference on Ecological Vehicles and Renewable Energies (EVER)*, Monte–Carlo, 2014, pp. 1–9.
- [14] Y. Gai *et al.*, “Cooling of automotive traction motors: Schemes, examples, and computation methods,” in *IEEE Transactions on Industrial Electronics*, vol. 66, no. 3, pp. 1681–1692, March 2019.
- [15] F. Ahmed, E. Ghosh, and N. C. Kar, “Transient thermal analysis of a copper rotor induction motor using a lumped parameter temperature network model,” *IEEE Transportation Electrification Conference and Expo*, 2016, pp. 1–6.
- [16] F. Ahmed and N. C. Kar, “Analysis of end–winding thermal effects in a totally enclosed fan–cooled induction motor with a die cast copper rotor,” in *IEEE Transactions on Industry Applications*, vol. 53, no. 3, pp. 3098–3109, May–June 2017.
- [17] D. Staton, A. Boglietti, and A. Cavagnino, “Solving the more difficult aspects of electric motor thermal analysis in small and medium size industrial induction motors,” in *IEEE Transactions on Energy Conversion*, vol. 20, no. 3, pp. 620–628, Sept. 2005.
- [18] Y. Gai *et al.*, “On the measurement and modeling of the heat transfer coefficient of a hollow–shaft rotary cooling system for a traction motor,” in *IEEE Transactions on Industry Applications*, vol. 54, no. 6, pp. 5978–5987, Nov–Dec. 2018.
- [19] B. Zhang, R. Qu, J. Wang, W. Xu, X. Fan, and Y. Chen, “Thermal model of totally enclosed water–cooled permanent–magnet synchronous machines for electric vehicle application,” in *IEEE Transactions on Industry Applications*, vol. 51, pp. 3020–3029, 2015.

- [20] D. G. Dorrell, D. A. Staton, J. Kahout, D. Hawkins, and M. I. McGilp, "Linked electromagnetic and thermal modeling of a permanent magnet motor," *3rd IET International Conference on Power Electronics, Machines and Drives-PEMD*, Dublin, Ireland, 2006, pp. 536–540.
- [21] S. Mezani, N. Takorabet, and B. Laporte, "A combined electromagnetic and thermal analysis of induction motors," in *IEEE Transactions on Magnetics*, vol. 41, no. 5, pp. 1572–1575, May 2005.
- [22] S. Mukundan, H. Dhulipati, J. Tjong, and N. C. Kar, "Parameter determination of PMSM using coupled electromagnetic and thermal model incorporating current harmonics," in *IEEE Transactions on Magnetics*, vol. 54, no. 11, pp. 1–5, Nov. 2018, Art no. 8110505.
- [23] O. Wallscheid and J. Böcker, "Global identification of a low-order lumped-parameter thermal network for permanent magnet synchronous motors," in *IEEE Transactions on Energy Conversion*, vol. 31, no. 1, pp. 354–365, March 2016.
- [24] O. Wallscheid and J. Böcker, "Design and identification of a lumped-parameter thermal network for permanent magnet synchronous motors based on heat transfer theory and particle swarm optimisation," *17th European Conference on Power Electronics and Applications (EPE'15 ECCE-Europe)*, Geneva, 2015, pp. 1–10.
- [25] Q. Lu, X. Zhang, Y. Chen, X. Huang, Y. Ye, and Z. Q. Zhu, "Modeling and investigation of thermal characteristics of a water-cooled permanent-magnet linear motor," in *IEEE Transactions on Industry Applications*, vol. 51, no. 3, pp. 2086–2096, May–June 2015.
- [26] J. Lindstrom, "Development of an experimental permanent-magnet motor drive," Chalmers University of Technology, Goteborg, Sweden, Rep. no. 312L, April. 1999.
- [27] A. M. EL-Refaie, N. C. Harris, T. M. Jahns, and K. M. Rahman, "Thermal analysis of multibarrier interior PM synchronous machine using lumped parameter model," in *IEEE Transactions on Energy Conversion*, vol. 19, no. 2, pp. 303–309, June 2004.
- [28] L. Zhiyong, W. Xuehuan, and C. Linhong, "Thermal analysis of PMSM based on lumped parameter thermal network method," *19th International Conference on Electrical Machines and Systems (ICEMS)*, Chiba, 2016.



- [29] B. Zhang, R. Qu, J. Wang, J. Li, W. Xu, and Y. Chen, “Electromagnetic–thermal coupling analysis of permanent magnet synchronous machines for electric vehicle applications based on improved ( $\mu+1$ ) evolution strategy,” in *IEEE Transactions on Magnetics*, vol. 51, no. 4, pp. 1–10, April 2015, Art no. 8104210.
- [30] P. Ponomarev, M. Polikarpova, and J. Pyrhönen, “Thermal modeling of directly–oil–cooled permanent magnet synchronous machine,” *XXth International Conference on Electrical Machines*, 2012, pp. 1882–1887.
- [31] B. Zhang, R. Qu, X. Fan, and J. Wang, “Thermal and mechanical optimization of water jacket of permanent magnet synchronous machines for EV application,” *IEEE International Electric Machines & Drives Conference*, Coeur d'Alene, 2015, pp. 1329–1335.
- [32] P. Ponomarev, M. Polikarpova, and J. Pyrhönen, “Conjugated fluid–solid heat transfer modeling of a directly–oil–cooled PMSM using CFD,” *Int. Symposium on Power Electronics Power Electronics, Electrical Drives, Automation and Motion*, Sorrento, 2012, pp. 141–145.
- [33] A. Nollau and D. Gerling, “Novel cooling methods using flux–barriers,” *International Conference on Electrical Machines*, Berlin, 2014, pp. 1328–1333.
- [34] A. Nollau and D. Gerling, “A flux barrier cooling for traction motors in hybrid drives,” *IEEE International Electric Machines & Drives Conference*, Coeur d'Alene, 2015, pp. 1103–1108.
- [35] A. Fatemi *et al.*, “Design of an electric machine for a 48–V mild hybrid vehicle,” *IEEE Energy Conversion Congress and Exposition*, Portland, OR, 2018, pp. 2278–2285.
- [36] Y. Zhang, S. McLoone, W. Cao, F. Qiu, and C. Gerada, “Power loss and thermal analysis of a MW high–speed permanent magnet synchronous machine,” in *IEEE Transactions on Energy Conversion*, vol. 32, pp. 1468–1478, Dec. 2017.
- [37] T. D. Kefalas and A. G. Kladas, “Thermal investigation of permanent–magnet synchronous motor for aerospace applications,” in *IEEE Transactions on Industrial Electronics*, vol. 61, pp. 4404–4411, 2014.

- [38] L. Hosain, R. B. Fdhila, and K. Ronnberg, "Air-gap flow and thermal analysis of rotating machine using CFD," *8<sup>th</sup> International Conference on Applied Energy (ICAE)*, Beijing, China 2016.
- [39] M. Kasprzak, J. W. Jiang, B. Bilgin, and A. Emadi, "Thermal analysis of a three-phase 24/16 switched reluctance machine used in HEVs," *IEEE Energy Conversion Congress and Exposition*, 2016, pp. 1–7.
- [40] J. Tang and Y. Liu, "Design and experimental verification of a 48 V 20 kW electrically excited synchronous machine for mild hybrid vehicles," *XIII International Conference on Electrical Machines*, Alexandroupoli, 2018, pp. 649–655.
- [41] M. Zeraouila, M. E. H. Benbouzid, and D. Diallo, "Electric motor drive selection issues for HEV propulsion systems: a comparative study," *IEEE Vehicle Power and Propulsion Conference*, Chicago, IL, 2005.
- [42] A. Boglietti, A. Cavagnino, M. Lazzari, and M. Pastorelli, "A simplified thermal model for variable-speed self-cooled industrial induction motor," in *IEEE Transactions on Industry Applications*, vol. 39, no. 4, pp. 945–952, July–Aug 2003.
- [43] E. Ghosh, F. Ahmed, A. Mollaeian, J. Tjong, and N. C. Kar, "Online parameter estimation and loss calculation using duplex neural—Lumped parameter thermal network for faulty induction motor," *IEEE Conference on Electromagnetic Field Computation*, 2016, pp. 1–1.
- [44] S. Mezani, N. Takorabet, and B. Laporte, "A combined electromagnetic and thermal analysis of induction motors," in *IEEE Transactions on Magnetics*, vol. 41, no. 5, pp. 1572–1575, May 2005.
- [45] A. Boglietti, A. Cavagnino, M. Parvis, and A. Vallan, "Evaluation of radiation thermal resistances in industrial motors," in *IEEE Transactions on Industry Applications*, vol. 42, no. 3, pp. 688–693, May–June 2006.
- [46] O. I. Okoro, "Steady and transient states thermal analysis of a 7.5-kW squirrel-cage induction machine at rated-load operation," in *IEEE Transactions on Energy Conversion*, vol. 20, no. 4, pp. 730–736, 2005.
- [47] C. Kral, A. Haumer, and T. Bauml, "Thermal model and behavior of a totally-enclosed-water-cooled squirrel-cage induction machine for traction applications,"

- in *IEEE Transactions on Industrial Electronics*, vol. 55, no. 10, pp. 3555–3565, Oct. 2008.
- [48] A. Boglietti, E. Carpaneto, M. Cossale, and S. Vaschetto, “Stator–winding thermal models for short–time thermal transients: Definition and validation,” in *IEEE Transactions on Industrial Electronics*, vol. 63, no. 5, pp. 2713–2721, May 2016.
- [49] C. Kral, A. Haumer, M. Haigis, H. Lang, and H. Kapeller, “Comparison of a CFD analysis and a thermal equivalent circuit model of a TEFC induction machine with measurements,” in *IEEE Transactions on Energy Conversion*, vol. 24, no. 4, pp. 809–818, Dec. 2009.
- [50] X. Wang, J. Du, G. Peng, and H. Lv, “Thermal comparison of a CFD analysis and a lumped parameter model of an air–cooled induction machine for EVs,” *International Journal of Applied Electromagnetics and Mechanics*, vol. 54, no. 1, pp. 37–56, 2017.
- [51] J. Gong, F. Gillon, and P. Brochet, “Magnetic and thermal 3D finite element model of a Linear Induction Motor,” *IEEE Vehicle Power and Propulsion Conference*, Lille, 2010, pp. 1–6.
- [52] R. Pechanek, V. Kindl, and B. Skala, “Transient thermal analysis of small squirrel cage motor through coupled FEA,” in *MM Science Journal*, pp. 560–563, 2015.
- [53] Z. Ye, W. Luo, W. Zhang, and Z. Feng, “Simulative analysis of traction motor cooling system based on CFD,” *International Conference on Electric Information and Control Engineering*, 2011, pp. 746–749.
- [54] M. Hettegger, B. Streibl, O. Biro, and H. Neudorfer, “Measurements and simulations of the convective heat transfer coefficients on the end windings of an electrical machine,” in *IEEE Transactions on Industrial Electronics*, vol. 59, no. 5, pp. 2299–2308, 2012.
- [55] Y. Zhang, J. Ruan, T. Huang, X. Yang, H. Zhu, and G. Yang, “Calculation of temperature rise in air–cooled induction motors through 3–D coupled electromagnetic fluid–dynamical and thermal finite–element analysis,” in *IEEE Transactions on Magnetics*, vol. 48, no. 2, pp. 1047–1050, 2012.
- [56] Z. Huang, F. Marquez, M. Alakula, and J. Yuan, “Characterization and application of forced cooling channels for traction motors in HEVs,” *XXth Int. Conf. on Electrical Machines*, 2012, pp. 1212–1218.

- [57] S. Moon, J. Yun, W. Kim, and J. Kim, “Thermal–flow analysis and cooling performance enhancement of a totally enclosed fan–cooled motor,” *International Conference on Electrical Machines and Systems*, Busan, 2013, pp. 2028–2030.
- [58] S. H. Moon, Y. H. Jung, and K. W. Kim, “Numerical investigation on thermal–flow characteristics of a totally enclosed fan cooled induction motor,” *XXII International Conference on Electrical Machines*, Lausanne, 2016, pp. 1928–1933.
- [59] C. Ulu, O. Korman, and G. Kömürgöz, “Electromagnetic and thermal analysis/design of an induction motor for electric vehicles,” *8th International Conference on Mechanical and Aerospace Engineering*, Prague, 2017, pp. 6–10.
- [60] A. Gudi, A. Singh, and B. Agarwal, “Electric machine stator thermal sensitivity analysis using CFD,” *IEEE Transportation Electrification Conference (ITEC–India)*, Pune, 2017, pp. 1–6.
- [61] D. Kim, D. Hong, J. Choi, Y. Chun, B. Woo, and D. Koo, “An analytical approach for a high speed and high efficiency induction motor considering magnetic and mechanical problems,” in *IEEE Transactions on Magnetics*, vol. 49, no. 5, pp. 2319–2322, May 2013.
- [62] N. Simpson, R. Wrobel, and P. H. Mellor, “A general arc–segment element for three–dimensional thermal modeling,” in *IEEE Transactions on Magnetics*, vol. 50, no. 2, pp. 265–268, Feb. 2014.
- [63] R. Wrobel and P. H. Mellor, “A general cuboidal element for three–dimensional thermal modeling,” in *IEEE Transactions on Magnetics*, vol. 46, no. 8, pp. 3197–3200, Aug. 2010.

# **CHAPTER 3**

## **LPTN MODELING FOR ONLINE TEMPERATURE PREDICTION OF PERMANENT MAGNET SYNCHRONOUS MOTOR FOR DIFFERENT DRIVE CYCLES IN ELECTRIC VEHICLE APPLICATIONS**

### ***3.1. Introduction***

Electric motor is the source of propulsion power in an electric vehicle and it must have the design characteristics including high torque at low speeds during starting and climbing, high power at high speeds during cruising, high instant power, high power density and efficiency, wide constant power speed range and high constant torque [1]. In addition, there are other factors including reliability, robustness, cost-effectiveness and compact structure [2] that influence the design criteria of the motor. Permanent Magnet Synchronous Motors (PMSM) are widely and commonly used as traction motors as they provide higher torque and power density with higher efficiency. High torque and power density would require higher current, which eventually results in higher heat generation in the motor. This active heat generation travels through different motor components and it affects the electromagnetic performance of the motor. Magnetic flux density and electromotive force significantly decrease with the increase of temperature of the motor. Also, the torque at high temperature is smaller than that at low temperature for the same speed of the motor. Temperature rise beyond a certain limit also causes the motor to demagnetize and stop operating [3]. Moreover, the traction motor must be compact and smaller structure, but high torque and power density requirements within the small structure contributes to high heat generation in the motor. Hence, it is critical to determine thermal characterization of the motor and ensure sufficient cooling to order to generate required torque and power. The performance of the traction motors is also affected by the driving conditions. In EV, standard tests for UDDS and HWFET are used to determine the performance of the traction motors in terms of torque, power, efficiency and thermal health. For example, in [5] interior permanent magnet synchronous motors were tested for both UDDS and HWFET drive cycles and identified that the traction motor must have to ensure proper cooling in order to provide and maintain required torque and power to satisfy both drive cycle conditions.

Now, it is critical to monitor the temperature of the traction motors accurately for each drive cycle condition so that proper coolant flowrate to the motor is regulated and maintained in order to generate required torque and power. Currently, direct measurement techniques are commonly used in the traction motor to monitor the temperature using resistance temperature detectors (RTDs) and thermocouples [6]. But it is extremely difficult to install these sensors and replace them when they are damaged [7]. On the other hand, heat is an accumulated effect that is caused by all different heat sources in the motor. In this case, thermal model-based temperature monitoring can ensure accurate prediction of temperature of the motor parts including stator winding and rotor magnet [8]. In the past, thermal models have been used to perform thermal analysis of the electric motor but those models have not considered drive cycle and dynamic cooling regulation. During driving conditions, the speed and torque fluctuate, which causes the variation in the temperature rise and as a result, the cooling requirement also varies. Hence, it is essential to consider driving conditions so that the model can give temperature results for various torque and speed requirements. This thesis proposes a simplified LPTN model where the motor loss model dynamically determines the motor losses based on the electromagnetic parameters and the LPTN model gives the temperature results based on the loss results. Although CFD and FEA have more accuracy in predicting heat and temperature in the motor, their computational time is much higher, which is absolutely not feasible in predicting motor temperature in driving conditions. The proposed LPTN model takes less time since it is an analytical model, and it regulates the cooling accordingly to produce required amount of torque and power by the traction motors in urban and highway driving conditions. This paper uses interior permanent magnet synchronous motors that are designed and built in the Centre for Automotive Research and Green Energy at the University of Windsor a leading research facility in transportation electrification. The proposed LPTN model is used to predict temperature for both the prototypes to determine motor temperature and demonstrate their thermal performance in order to provide torque and power required by varying load cycles for the UDDS and HWFET.

### ***3.2. Targeted Traction Motors and Drive Cycle Overview***

In this research, two interior permanent magnet synchronous motors were tested for their thermal performance. IPMSM prototype A and prototype B are shown in the Figure 3.1.

Table 3.1 describes technical specifications of the prototypes and Table 3.2 describes physical dimensions and parameters that are used in the proposed LPTN thermal modeling.

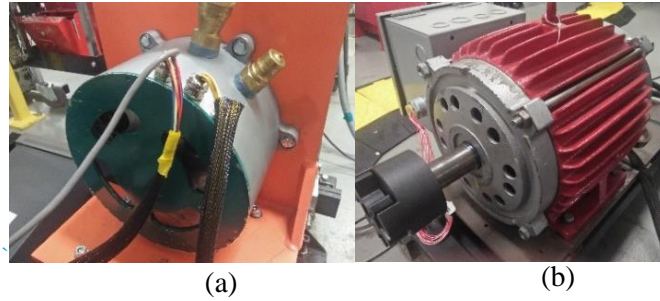


Figure 3.1. IPMSM prototype motors designed for EV. (a) Prototype A. (b) Prototype B.

Table 3.1. Technical Specifications of the IPMSMs

Parameters	Prototype A	Prototype B
Rated output power	22 kW	4.25 Kw
Rated voltage	275 V	275 V
Rated torque	70 Nm	70 Nm
Rated speed	3,000 rpm	575 RPM
Continuous phase current	78 A	11 A rms
Type of steel	M19_29G	M19_29G
Type of magnet	NdFe35	NDFEB35@100

Table 3.2. Physical Parameters of the IPMSMs

Parameters	Prototype A	Prototype B
Inner diameter of stator	134 mm	135 mm
Outer diameter of stator	195 mm	220 mm
Stator stack length	75 mm	136 mm
Air-gap thickness	0.5 mm	0.5 mm
Outer rotor diameter	133	134 mm
Length of rotor core	75 mm	136 mm
Thickness of magnet	3 mm	3.81mm
Width of magnet	20 mm	25.4 mm
Shaft radius	50 mm	42.5 mm
Weight of copper	1.74 kg	3.76 kg
Weight of stator core	6.2 kg	19.6 kg
Weight of rotor core	2.88 kg	7.12 kg
Weight of magnet	0.53 kg	0.615 kg

Figure 3.2 shows the torque-speed characteristics of the prototype A and prototype B. Prototype A shows the design and peak torque and speed characteristics and prototype B shows only rated or design torque speed characteristics of the motor. Both UDDS and

HWFET driving conditions are plotted in the graph to describe the relationship between the motor capacity to produce torque and power under urban and highway driving conditions. Prototype A has a greater capacity and it covers the full spectrum of the driving conditions under UDDS and HWFET drive cycles.

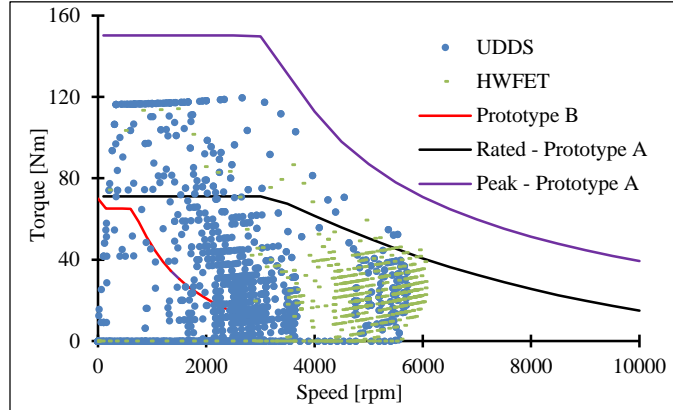


Figure 3.2. Torque–speed graph for prototype A and prototype B.

On the other hand, prototype B is a scale–down prototype motor to demonstrate its electromagnetic and thermal performance. LPTN thermal model is developed for each of the motor prototype to determine stator winding temperature under varying loading conditions. Only prototype B is used to validate the LPTN model in this work.

### 3.3. Proposed Lumped Parameter Thermal Network (LPTN) Model

#### 3.3.1. LPTN Model Overview

Lumped Parameter Thermal Network (LPTN) is a thermal network that describes the heat transfer phenomenon in a system. LPTN model for PMSM consists of the motor components as nodes and each node indicates the temperature of the respective component. The paths of heat flow are taken as thermal resistances that depend on the temperature difference between the nodes. The LPTN model proposed as shown in Figures 3.3 and 3.4 that include the motor components such as stator, rotor, magnet, winding and casing. The conduction and convection heat transfer processes take place in various motor components which are indicated by thermal resistances and temperature nodes in the network and the heat losses of the motor are considered as sources of heat.  $T_1$  indicates rotor temperature,  $P_{cu-eddy}$  is the rotor core loss,  $C_1$  is the thermal capacitance of rotor core,  $R_1$  is the thermal resistance for conduction through rotor core,  $T_2$  is the magnet temperature,  $P_{mag}$  is the



magnet loss,  $C_2$  is the thermal capacitance of magnet,  $R_2$  is the thermal resistance for conduction through magnet,  $T_3$  is the air-gap temperature,  $R_3$  is the thermal resistance for convection through air-gap,  $T_4$  is the stator teeth temperature,  $P_{cu-s}$  is the stator copper loss,  $C_3$  is the thermal capacitance of stator teeth,  $R_4$  is the thermal resistance for conduction through stator teeth and winding,  $C_4$  is the thermal capacitance of stator core,  $P_{lam}$  is the stator core loss,  $T_5$  is the stator winding temperature,  $R_5$  is the thermal resistance for conduction through stator core,  $T_6$  is the temperature of stator core,  $C_{casing}$  is the thermal capacitance of casing steel,  $R_6$  is the thermal resistance for convection from end-winding,  $R_7$  is the thermal resistance for convection from inner air,  $P_{coolant}$  is the amount of heat removal,  $R_8$  is the thermal resistance for conduction through casing,  $R_9$  is the thermal resistance for convection from casing. Heat losses are taken as input from the loss models in MATLAB Simulink and then the thermal the resistances and heat transfer coefficients are obtained analytically from geometry information. The LPTN model was built for Interior Permanent Magnet Synchronous Motor (IPMSM) and the necessary parameters of the motors are given in tables 4.1 and 4.2. Based on the data, the analytical calculation was performed.

### 3.3.2. Analytical Solution of LPTN Model

LPTN model uses energy conservation equations at each node for describing the heat transfer phenomenon at that node. The rate of change of energy at a node is the sum of all heat transfers including conduction, convection and radiation modes, as well as the motor loss. Thermal resistances of all the components are required for evaluating the heat transfer.

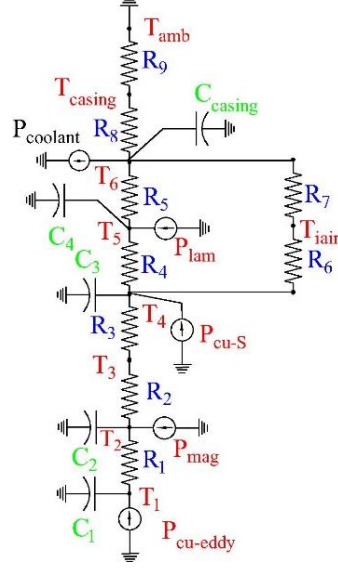


Figure 3.3. Proposed simplified lumped parameter thermal network.

Thermal resistance for convection from the motor casing to the ambient is given by equation (3.1)

$$R = \frac{1}{A_{casing} \times h_{casing}} \quad (3.1)$$

where  $A_{casing}$  is the area of the motor casing and  $h_{casing}$  is the heat transfer coefficient for forced convection from casing to ambient. The casing has fins and the heat transfer coefficient for convection from casing to ambient can be calculated as

$$h = \frac{(\rho C_p D_h v_{fin})}{[4 \times L_{fin} \times (1 - e^{-m})]} \quad (3.2)$$

where  $L_{fin}$  is the length of the fins (in the axial direction),  $D_h$  is the hydraulic diameter and  $v_{fin}$  velocity of air in the fin channels, and

$$m = \frac{0.1448 L_{fin}^{0.946}}{D_h^{1.16} \times \left( \frac{h_{fin}}{\rho C_p v_{fin}} \right)^{0.214}} \quad (3.3)$$

where  $\rho$  is the density of air and  $C_p$  is the thermal capacitance of air [9].

The convection heat transfer through the air-gap has a thermal resistance given by equation (3.4)

$$R = \frac{1}{A_{rotor} h_{air-gap}} \quad (3.4)$$

where  $A_{rotor}$  is the curved surface area of the rotor from where convection occurs and  $h_{air-gap}$  the convection heat transfer coefficient in the air-gap, which is further given by equation

(3.5).

$$h_{air-gap} = \frac{Nu \times K_{air}}{l_{air-gap}} \quad (3.5)$$

Here,  $Nu$  is the Nusselt number,  $K_{air}$  is the thermal conductivity of air, and  $l_{air-gap}$  is the thickness of air-gap. The Nusselt number can be found from the following equations (3.6)–(3.8) depending on the value of the modified Taylor number [8].

$$Nu = 2 \quad (for \ Ta_m < 1,700) \quad (3.6)$$

$$Nu = 0.128 \ Ta_m^{0.367} \quad (for \ 1,700 < Ta_m < 10^4) \quad (3.7)$$

$$Nu = 0.409 \ Ta_m \quad (for \ 10^4 < Ta_m < 10^7) \quad (3.8)$$

Here,  $Ta_m$  is the modified Taylor number obtained by equation (3.9).

$$Ta_m = \frac{Ta}{F_g} \quad (3.9)$$

Here,  $Ta$  is the Taylor number and  $F_g$  is the geometrical factor. Taylor number is found from equation (3.10)

$$Ta = \frac{\rho^2 \omega^2 r_m l_{air-gap}^2}{\mu^2} \quad (3.10)$$

where  $\rho$  is the density of air,  $\omega$  is the rotational speed of the rotor,  $r_m$  is the average of stator radius and rotor radius, and  $\mu$  is the dynamic viscosity of air. However, since the air-gap thickness  $l_{air-gap}$  is very small, the  $F_g$  is considered to be 1, which makes  $Ta_m$  equal to  $Ta$  [8].

The conduction heat transfer through the rotor core has a thermal resistance given by equation (3.11)

$$R = \frac{1}{2\pi k_{rotor} l_{rotor}} \ln \left( \frac{r_{rotor-outer}}{r_{rotor-inner}} \right) \quad (3.11)$$

Here,  $k_{rotor}$  is the thermal conductivity of rotor material,  $l_{rotor}$  is the length of the rotor core,  $r_{rotor-outer}$  is the outer radius of rotor and  $r_{rotor-inner}$  is the inner radius of rotor.

The thermal resistance for conduction heat transfer through the interior magnet is given by equation (3.12).

$$R = \frac{1}{n\theta k_{magnet} l_{magnet}} \ln \left( \frac{r_{rotor}}{r_{magnet}} \right) \quad (3.12)$$

where  $n$  is the number of poles,  $\theta$  is the angle of each pole in radians,  $k_{magnet}$  is the thermal conductivity of magnet,  $l_{magnet}$  is longitudinal length of the magnets,  $r_{rotor}$  is the outer radius of rotor and  $r_{magnet}$  is the radius till the inner surface of the magnet.

The conduction through the stator can be divided into two parts such as the conduction through stator winding and teeth, and the conduction through the stator core. The conduction through stator winding and teeth has a thermal resistance given by equation (3.13).

$$R = \frac{1}{2\pi k_{stator} l_{stator} p} \ln \left( \frac{r_{stator-slot}}{r_{stator-inner}} \right) \quad (3.13)$$

where  $k_{stator}$  is the thermal conductivity of stator,  $l_{stator}$  is the stator stack length,  $p$  is the ratio of the area of teeth section to the total area of teeth and slots,  $r_{stator-slot}$  is the radius till the outer surface of the slots and  $r_{stator-inner}$  is the inner radius of stator.

The conduction through stator core has a thermal resistance given by equation (3.14).

$$R = \frac{1}{2\pi k_{stator} l_{stator}} \ln \left( \frac{r_{stator-yoke-outer}}{r_{stator-yoke-inner}} \right) \quad (3.14)$$

Here,  $K_{stator}$  is the thermal conductivity of stator,  $l_{stator}$  is the stator stack length,  $r_{stator-yoke-outer}$  is the outer radius of stator yoke and  $r_{stator-yoke-inner}$  is the inner radius of stator yoke.

### 3.3.3. Motor Loss Approximations for LPTN Model–Prototypes A and B

Motor prototypes were designed in ANSYS and through electromagnetic simulation, the losses are generated for varying loading torque and speed conditions. Figures. 3.5 and 3.6 show the major losses in the prototype A and prototype B.

As shown in Figure 3.2 for prototype A, the torque generation for the UDDS drive cycle lies between the rated and peak torque–speed conditions and required torque generation for HWFET drive cycle lies below the rated torque–speed conditions. Table 3.3 shows the losses for the selected operating points from torque–speed characteristics where 500 rpm and 2,500 rpm are the requirements for UDDS conditions and 5,000 rpm and 8,000 rpm are the requirements for HWFET conditions.

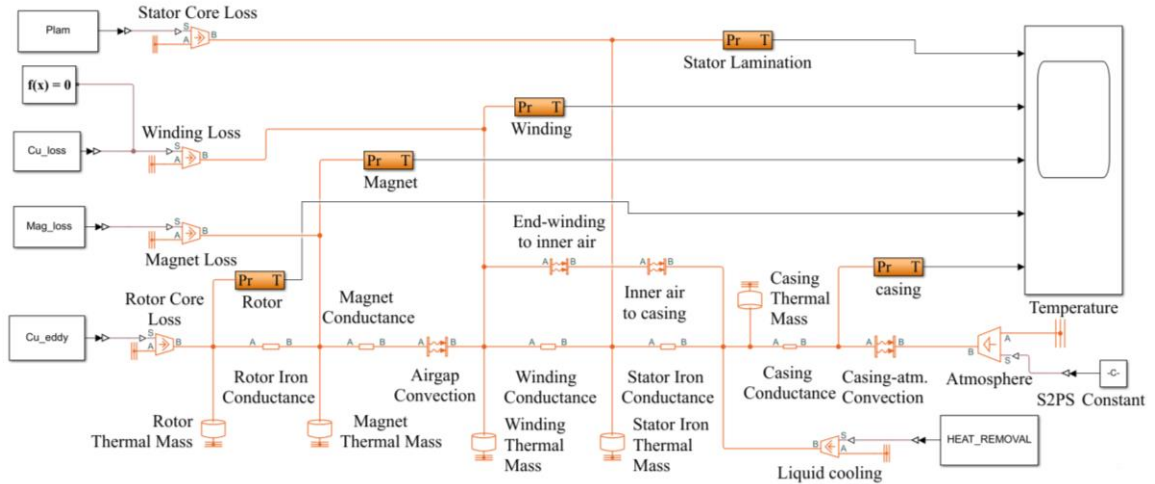


Figure 3.4. Simplified LPTN model in MATLAB Simulink to determine thermal characterization of the motor.

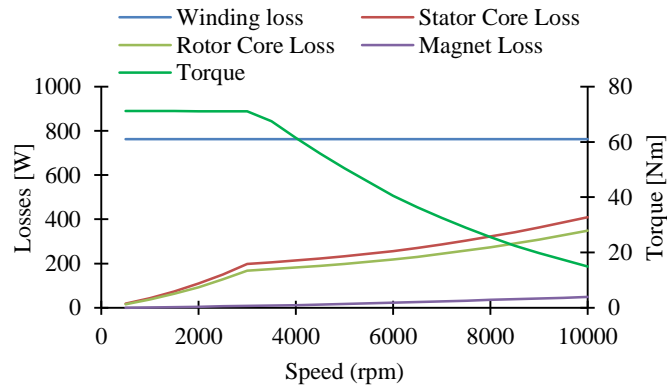


Figure 3.5. Major losses from the IPMSM prototype A for varying torque and speed conditions.

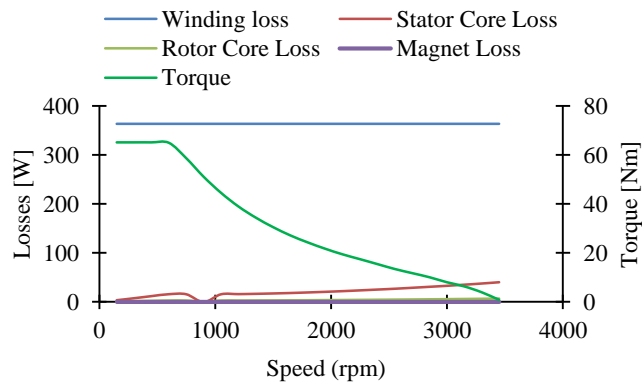


Figure 3.6. Major losses from the IPMSM prototype B for varying torque and speed conditions.

The loss values for these operating points will be used in the LPTN model for prediction of thermal health of the motor. There are some operating points under UDDS drive cycles that does not cover by the torque generation by prototype A at rated condition. However, predicted thermal status for the rated condition under UDDS and HWFET will indicate overall thermal status and required cooling.

Table 3.3. Selected Losses from Prototype A for UDDS and HWFET Conditions

Speed (rpm)	500	2,500	5,000	8,000
Torque (Nm)	71	71	50	25
Stator core loss (W)	16.31	128.26	197.78	273.86
Rotor core loss (W)	2.88	22.63	34.9	48.33
Magnet loss (W)	0.4145	6.55	17.18	35.64
Total loss (W)	782.67	920.5	1012.93	1120.9
90% of total loss (W)	704.4	828.45	911.64	1008.8
80% of total loss (W)	626.13	736.4	810.34	896.71

Table 3.4. Selected Losses from Prototype B for UDDS Conditions

Speed (rpm)	300	600	1,200	1,500
Torque (Nm)	65	65	39	31
Stator core loss (W)	7.81	16.03	16.2	17.56
Rotor core loss (W)	1.38	2.83	2.86	3.1
Magnet loss (W)	0.0106	0.0413	0.1086	0.1313
Total loss (W)	372.2	381.9	382.15	383.8
90% of total loss (W)	335	343.7	344	345.4
50% of total loss (W)	186.1	190.9	191.1	191.9

As shown in Figure 3.2, prototype B only covers partly below under UDDS condition. This prototype is a scale-down IPMSM traction motor design which will be used primarily to validate the proposed thermal model as well as justify the cooling requirements compared to the prototype A. For prototype A, Table 3.3 shows the values of 90% and 80% of the total loss and for prototype B, Table 3.4 shows 90% and 50 % of the total loss. These different percentage of losses will be used in LPTN model as the amount of heat removal from the motor using liquid cooling. This will demonstrate that LPTN will predict the stator winding temperature when prototype A will expel the amount of heat equivalent to 90% or 80% of the total motor loss.

### 3.4. Heat Removal by Liquid Cooling

The LPTN model has then been modified as shown in Figure 3.7. Heat removal block is replaced by motor cooling channel block and radiator cooling pipe block. The cooling blocks have been implemented in order to incorporate the coolant flow rate required. Water-glycol is used as the liquid coolant. The amount of heat removed from stator can be written as:

$$\dot{Q} = hA_{conv}(T_{stator} - T_{water-glycol}) \quad (3.15)$$

which is the same amount of heat absorbed by water-glycol and can be written as:

$$\dot{Q} = \dot{m}C_p (T_{outlet} - T_{inlet}) \quad (3.16)$$

Here,  $h$  is a convection coefficient,  $A_{conv}$  is convection area,  $T_{stator}$  is stator temperature,  $T_{water-glycol}$  is water-glycol temperature,  $\dot{m}$  is mass flow rate of water-glycol,  $C_p$  is a specific heat of water-glycol,  $T_{outlet}$  is water-glycol temperature at motor outlet,  $T_{inlet}$  is water-glycol temperature at motor inlet.

The convection coefficient can be calculated from:

$$h = \frac{k_f \times Nu}{D} \quad (3.17)$$

where  $k_f$  is thermal conductivity of water-glycol and  $D$  is hydraulic diameter of cooling channel.

Nusselt number needs to be determined in order to find the  $h$ . So, Nusselt number can be found from the following equations at different conditions.

For turbulent flow,

$$Nu = \frac{f}{8} \times \frac{(Re-1000) \times Pr}{1 + 12.7 \times \left(\frac{f}{8}\right)^{0.5} \times (Pr^{2/3} - 1)} \quad (3.18)$$

where  $Re$  = Reynolds number,  $Pr$  = Prandtl number and  $f$  is the friction factor calculated as a function of Reynolds number.

$$f = [0.790 \times \ln(Re) - 1.64]^{-2} \quad (3.19)$$

For laminar flow in round channels,

$$Nu = 3.66 + \frac{0.065 \times (D/L) \times Re \times Pr}{1 + 0.04 \times \{(D/L) \times Re \times Pr\}^{2/3}} \quad (3.20)$$

For laminar flow in concentric channels,

$$Nu = 7.54 + \frac{0.03 \times (D/L) \times Re \times Pr}{1 + 0.016 \times \{(D/L) \times Re \times Pr\}^{2/3}} \quad (3.21)$$

For laminar flow in rectangular channels,

$$Nu = 7.49 - 17.02 \times \frac{H}{W} + 22.43 \left(\frac{H}{W}\right)^2 - 9.94 \times \left(\frac{H}{W}\right)^3 + \frac{0.065 \times (D/L) \times Re \times Pr}{1 + 0.04 \times \{(D/L) \times Re \times Pr\}^{2/3}} \quad (3.22)$$

where  $D$  is hydraulic diameter of cooling channel,  $L$  is Length of cooling channel,  $H$  is Height of cooling channel,  $W$  is Width of cooling channel,  $Re$  is Reynolds number, and  $Pr$  is Prandtl number.

Equation (3.18) has to be used for turbulent flow in any type of channel geometry. On the other hand, equations (3.20) – (3.22) have to be used for laminar flow in the respective type of channel geometry. The flow is defined to be laminar if the  $Re < 4,000$  and turbulent if  $Re > 4,000$ .

Aggregate length of local resistance was found from the minor loss coefficient which is dependent on geometry.

$$K = \frac{L}{v^2 / 2g} \quad (3.23)$$

Reynolds number coefficient was found from empirical Reynolds number relationship based on width–to–height ratio in rectangular geometry.



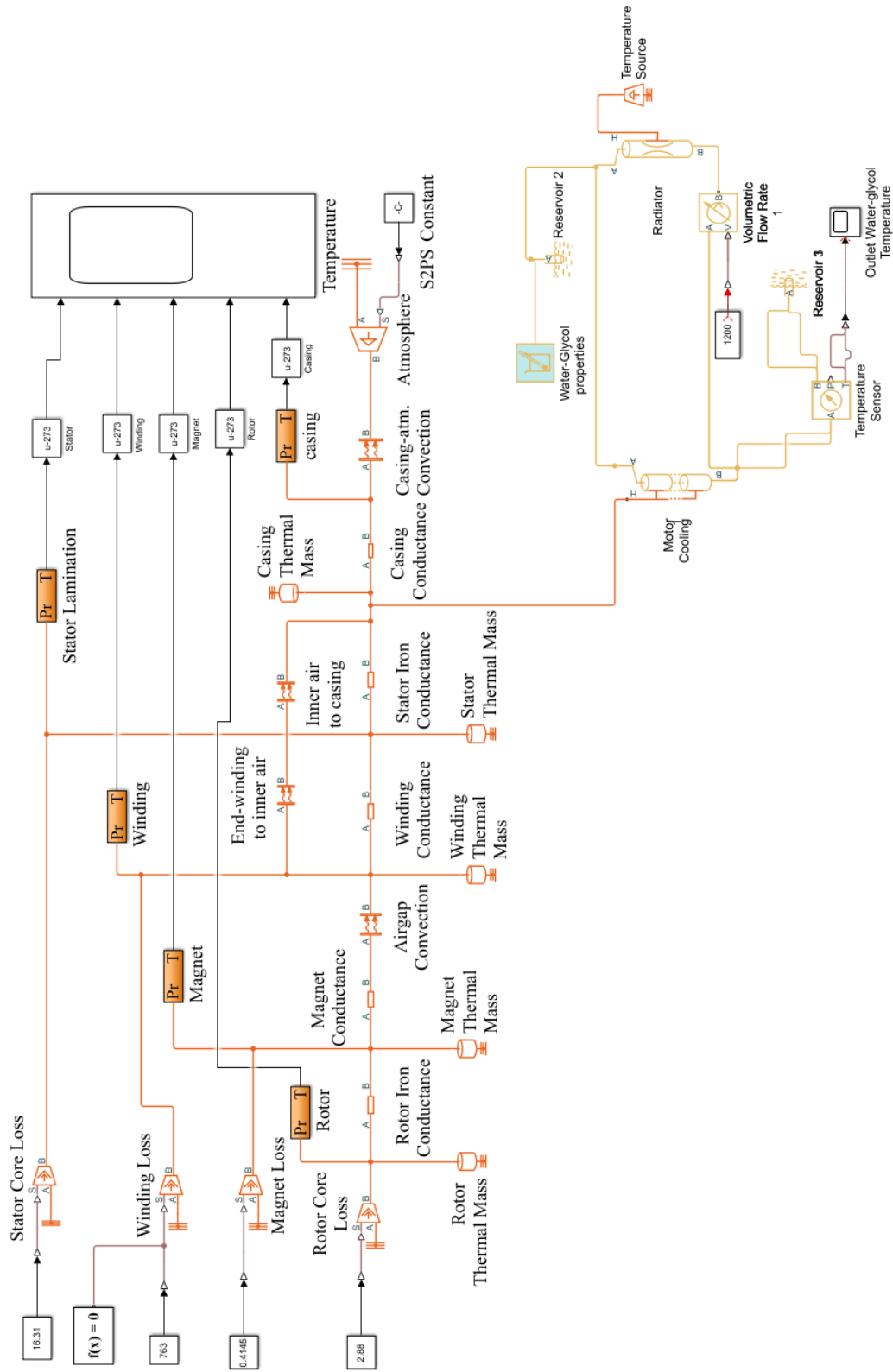


Figure 3.7. Modified LPTN model with cooling blocks.

The parameters in the cooling channel block have been setup in the Simulink model.

Configuration	Viscous Friction	Heat Transfer	Initial Conditions
Fluid dynamic compressibility:	Off		
Pipe total length:	3.2987	m	▼
Nominal cross-sectional area:	0.1	m <sup>2</sup>	▼
Hydraulic diameter:	0.01	m	▼
Elevation gain from port A to port B:	0	m	▼
Gravitational acceleration:	9.81	m/s <sup>2</sup>	▼

(a)

Configuration	Viscous Friction	Heat Transfer	Initial Conditions
Viscous friction parameterization:	Haaland correlation		
Aggregate equivalent length of local resistances:	0.33	m	▼
Internal surface absolute roughness:	4.6e-5	m	▼
Laminar friction constant for Darcy friction factor:	82		
Laminar flow upper Reynolds number limit:	2e+3		
Turbulent flow lower Reynolds number limit:	4e+3		

(b)

Configuration	Viscous Friction	Heat Transfer	Initial Conditions
Heat transfer parameterization:	Gnielinski correlation		
Nusselt number for laminar flow heat transfer:	3.6		

(c)

Configuration	Viscous Friction	Heat Transfer	Initial Conditions
Initial liquid temperature:	25	degC	▼

(d)

Figure 3.8. Parameter setup in Simulink model.

### 3.5. Experimental Setup for Thermal Tests

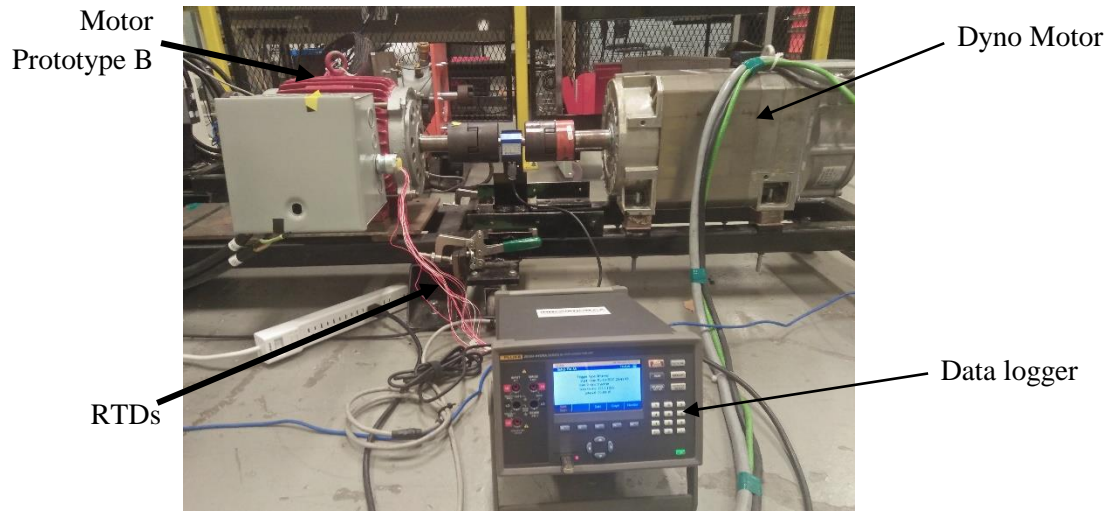


Figure 3.9. Experimental setup for thermal tests for prototype B.

Experimental setup with IPMSM motor prototype B is shown in Figure 3.9. Power was supplied to a dyno motor which was used for driving the motor prototype B. Resistance temperature detectors (RTDs) were embedded in the stator end-windings of the prototype for measuring the temperature. Data logger recorded the data found from the RTDs.

### 3.6. Results and Analysis

IPMSM motor prototypes A and B were used for both UDDS and HWFET driving conditions to predict stator winding temperature of the motor using the proposed simplified LPTN model. Motor prototype A is built but it is not in a state of operation at this point, hence, only simulation results from LPTN are presented for prototype A. Prototype B has been used both for simulation and experimental validation of LPTN model results.

#### 3.6.1. Simulations Results from the LPTN Model–IPMSM Prototype A

Stator winding temperature for 500 rpm and 65 Nm loading conditions are shown in Figure 3.10. When no cooling at all is used for the prototype A, the stator winding temperature rise is around 670°C. This is absolutely high temperature for the motor and active liquid cooling is required. LPTN model uses the cooling block that removes 90% and 80% equivalent amount of heat from the motor that results the temperature rise in the stator winding are 90°C and 162°C respectively. In this case, 90% heat removal from the motor predicts the temperature lower than the motor insulation design limit of 110°C. Hence, the

cooling channel in the motor must remove the heat of 90% equivalent to the total loss in order to keep 90°C. On the other hand, 80% cooling will never be possible to bring down the temperature of the motor to the design limit. Moreover, the operating point here considered is 500 rpm and rated torque of 65 Nm. There are some operating points below UDDS beyond these rated conditions and requires higher torque, which eventually will generate more heat in the motor. As a result, cooling condition will restrict the motor prototype A to run longer period of time beyond these operating limits. The temperature results from LPTN simulation for different motor components are shown in Figure 3.11.

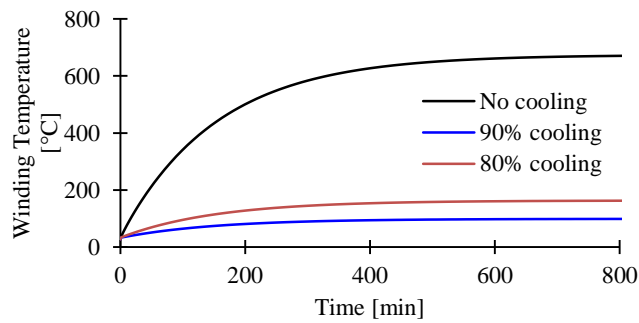


Figure 3.10. Stator winding temperature results from LPTN model for prototype A under 500 rpm and rated torque of 65 Nm condition.

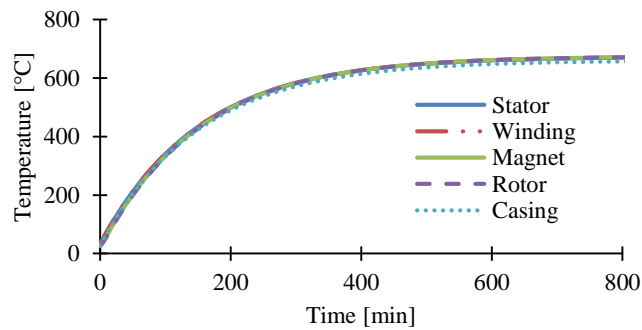


Figure 3.11. Temperature results from LPTN model for prototype A under 500 rpm and rated torque of 65 Nm condition.

Ideally, the different motor components should have different temperature values because they are made of different materials and their configurations are also different. However, the prototype A is a very small motor with an outer diameter of 195 mm and an axial length of 75 mm. It has a very high phase current of 78 A within such a small volume, which causes a very high amount of heat generation within the motor. This very high value of heat within such a small motor eventually results in a high heat density and a quick heat transfer, which leads to a steady state where all the motor components are nearly in a thermally equilibrium state. That is why Figure 3.11 shows all the motor components to have approximately the same temperature.

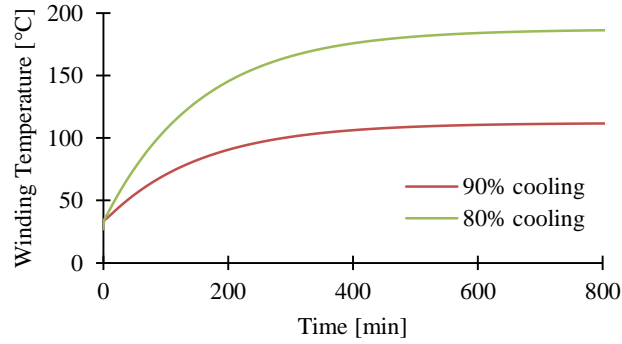


Figure 3.12. Stator winding temperature results from LPTN model for prototype A under 2,500 rpm and rated torque of 71 Nm condition.

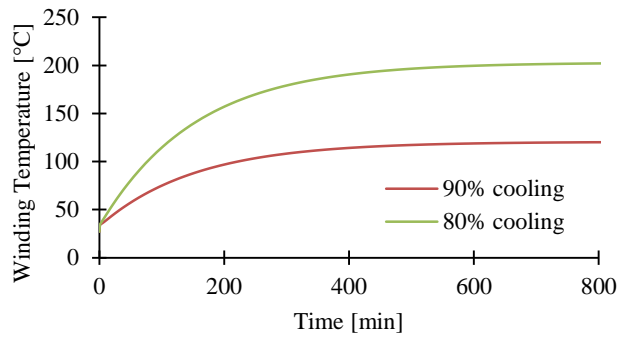


Figure 3.13. Stator winding temperature results from LPTN model for prototype A under 5,000 rpm and rated torque of 50 Nm condition.

Stator winding temperature rise for 2,500 rpm and with 90% and 80% cooling are 111°C and 186°C respectively, as presented in Figure 3.12. This operating 500 point is still below UDSS and temperature rise went up compared to rpm condition for prototype A. HWFET driving condition is represented in Figure 3.13, where the temperature rise of the stator winding with 90% and 80% cooling are 120°C and 202°C respectively. It is clearly demonstrated that 80% cooling is never sufficient for prototype A for UDSS and HWFET driving conditions as shown in Figure 3.13. A comparison of the temperature rise for 500 rpm, 2,500 rpm and 5,000 rpm with 80% and 90% cooling requirement is stated in Figures 3.14 and 3.15 respectively. The highest temperature of the stator winding rises to 120°C with 90% cooling. Hence, LPTN predicted winding temperature is in the ranges from 90°C to 120°C to satisfy both UDSS and HWFET conditions except that some points identified beyond rated torque.

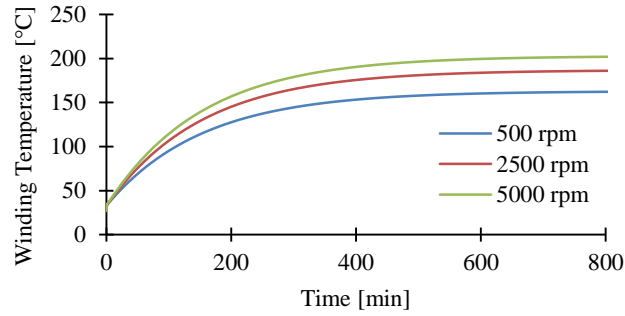


Figure 3.14. Stator winding temperature results from LPTN model for prototype A under 500 rpm, 2500 rpm and 5,000 rpm with 80% cooling.

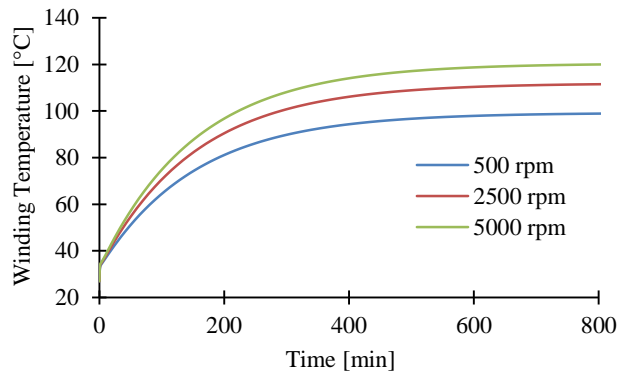


Figure 3.15. Stator winding temperature results from LPTN model for prototype A under 500 rpm, 2,500 rpm and 5,000 rpm with 90% cooling.

### 3.6.2. Simulations Results from the LPTN Model–IPMSM Prototype B

The temperature results from LPTN simulation for different motor components are mentioned in Figure 3.16. The winding temperature rise for prototype B with no cooling is around 100°C, which is below than the winding insulation design temperature of 120°C, as shown in Figure 3.17. This is a scale-down motor prototype that demonstrates better thermal condition of the motor. Hence, the electromagnetic design parameters can be followed in order to scale up the design of the IPMSM traction motor. With 90% cooling the stator winding temperature is around 40°C which is much lower temperature. This demonstrates that it is not required to design any cooling for this prototype to remove 90% of heat from the motor. With 50% cooling the winding temperature is 65°C, which is much ideal operating condition for the traction motor. Similar winding temperature and cooling requirements for the prototype even at higher speed conditions are demonstrated in Figures 3.18 and 3.19. Hence, only 50% cooling design would be the sufficient for this prototype

B. The scale-up design will demand higher torque and power requirements; however, the design parameters of this prototype can be useful for traction motor design in the future.

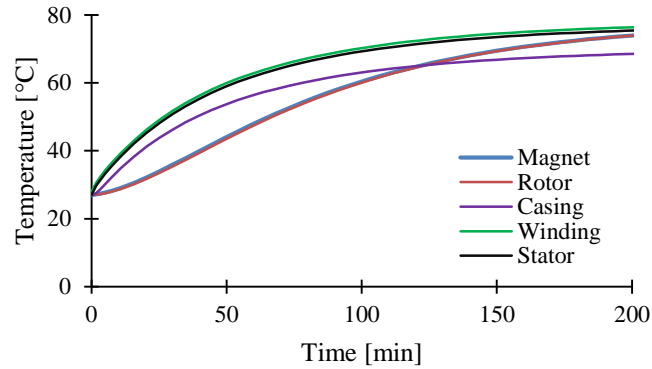


Figure 3.16. Temperature results from LPTN model for prototype B under 300 rpm and rated torque of 65 Nm condition.

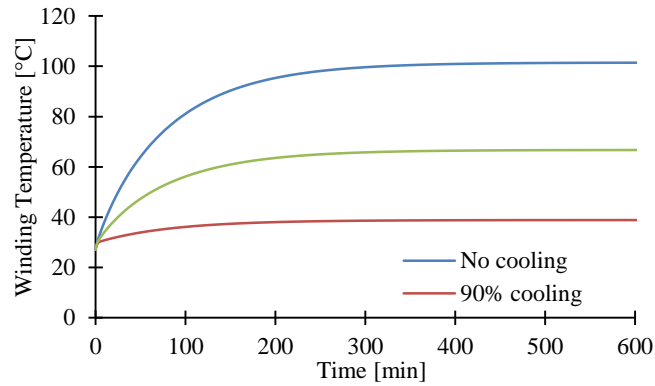


Figure 3.17. Stator winding temperature results from LPTN model for prototype B under 300 rpm and rated torque of 65 Nm condition.

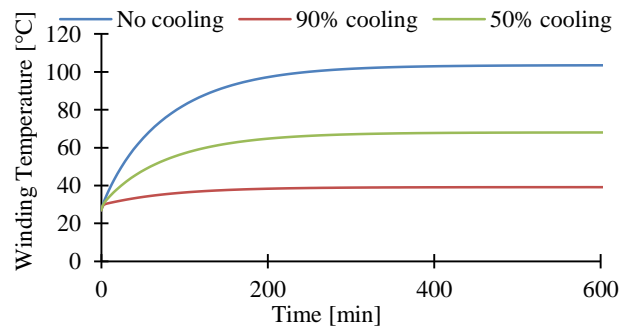


Figure 3.18. Stator winding temperature results from LPTN model for prototype B under 600 rpm and rated torque of 65 Nm condition.

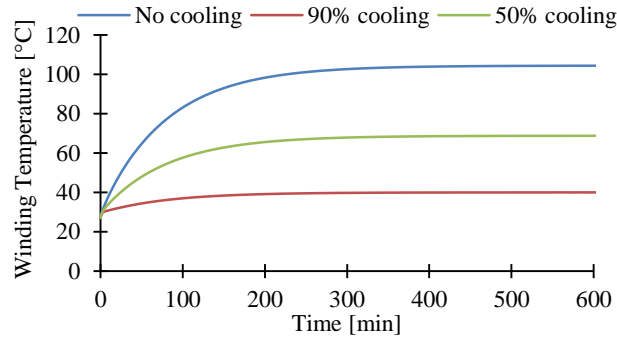


Figure 3.19. Stator winding temperature results from LPTN model for prototype B under 1500 rpm and rated torque of 31 Nm condition.

### 3.6.3. Experimental Validation of Temperature Results from LPTN Simulation

Thermal tests were performed on the motor prototype B under varying loading and speed conditions. Winding temperature for 100 rpm and with 40 Nm and 57 Nm loading is given in Figure 3.20. Winding temperature for 300 rpm and with 49 Nm and 65 Nm loading is presented in Figure 3.21. No cooling was used for the thermal tests. The prototype does not consist any cooling channel. The heat generation in the motor is completely dissipated through the casing. Liquid cooling was only simulated for both motor prototypes. A comparison of the LPTN model results and experimental model results for the prototype B has been mentioned in Figures 3.22–3.25. The results compare very well with simulation results and validate the LPTN model. Magnet temperatures which were measured by using thermal imager at the end of two-hour period of each experiment are shown in Figures 3.26 and 3.27.

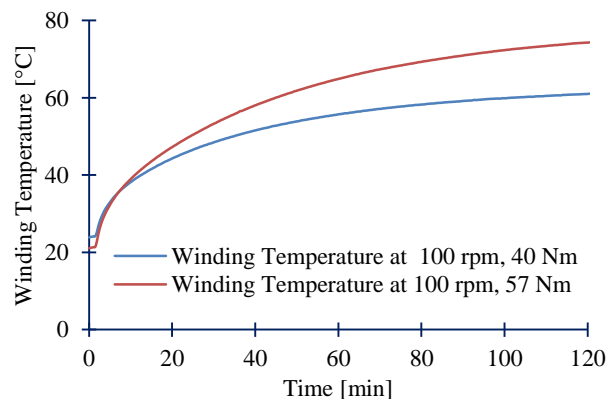


Figure 3.20. Winding temperature from experiments at 100 rpm for 40 Nm and 57 Nm torque.



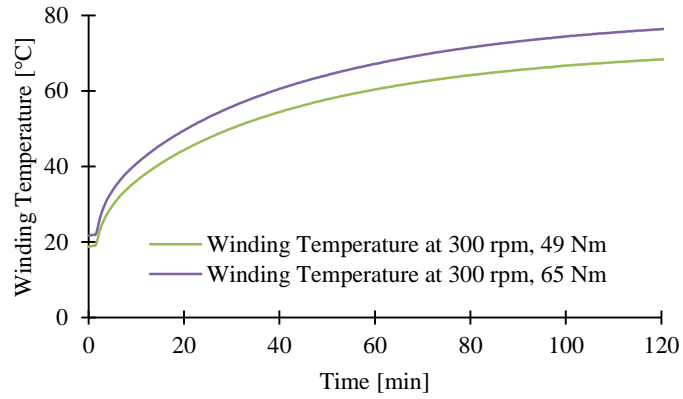


Figure 3.21. Winding temperature from experiments at 300 rpm for 49 Nm and 65 Nm torque.

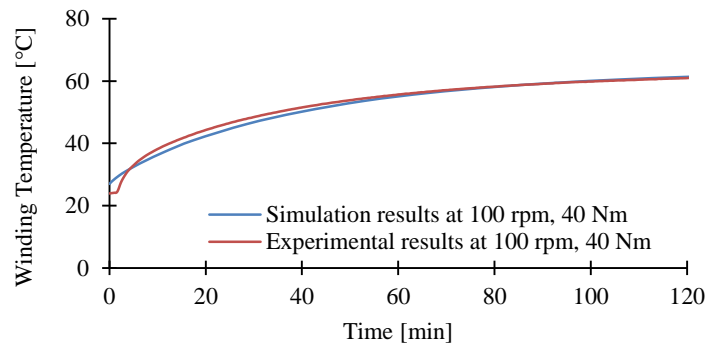


Figure 3.22. Comparison between experimental and simulation results at 100 rpm and 40 Nm.

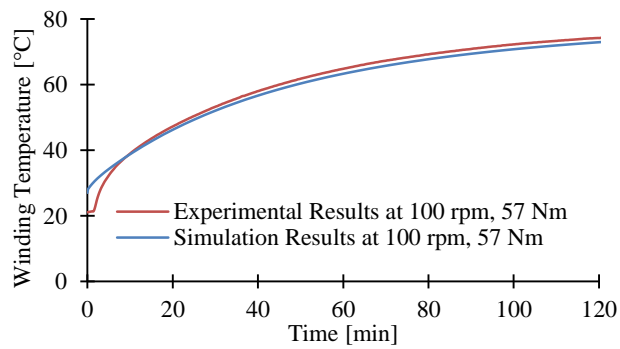


Figure 3.23. Comparison between experimental and simulation results at 100 rpm and 57 Nm.

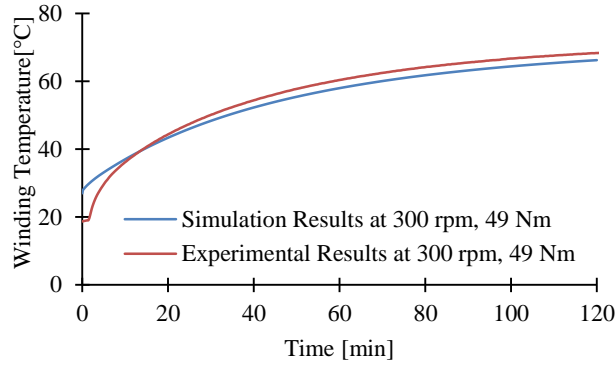


Figure 3.24. Comparison between experimental and simulation results at 300 rpm and 49 Nm.

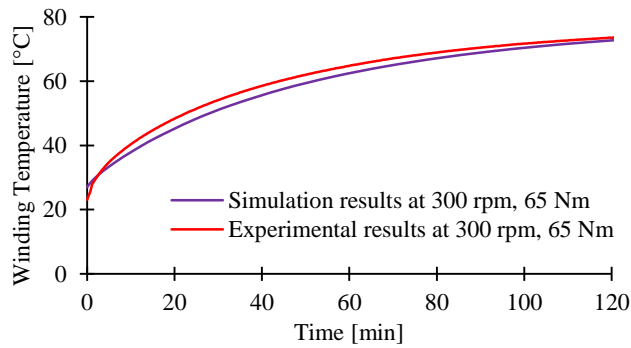


Figure 3.25. Comparison between experimental and simulation results at 300 rpm and 65 Nm.

The difference between simulated results and experimental results for motor winding temperature has been caused by the precision error of the RTDs used in the experimental setup. The calculation of convection coefficient from Taylor number may also have caused an error, which has to be further investigated.

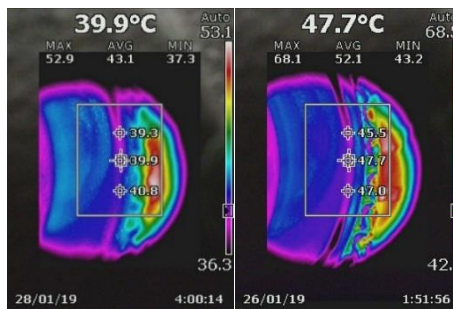


Figure 3.26. Magnet temperature at 44 and 58 Nm respectively at 100 rpm.

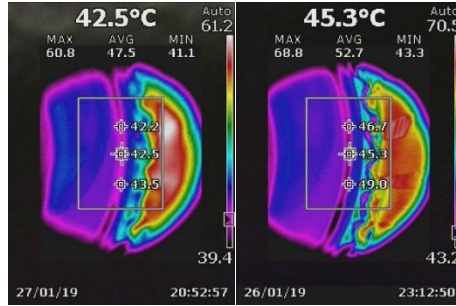


Figure 3.27. Magnet temperature at 49 and 65 Nm respectively at 300 rpm.

### 3.7. Conclusion

Motor prototypes A and B are designed for traction motor applications. Prototype A is designed primarily full scale to be used in EV. The proposed LPTN model is used to determine winding temperature for prototype A for varying operating points of the torque–speed characteristics under UDDS and HWFET drive cycles. The produced LPTN results demonstrate the cooling requirements in the motor in order to produce required torque for varying drive conditions. Prototype B was used primarily to validate the proposed LPTN model. Experimental results agree well with the simulation results for prototype B. Hence, the proposed thermal model developed and validated in this work will be very useful in automotive industry to determine thermal characterization of the traction motor under varying drive conditions. In order to predict stator winding temperature dynamically using the proposed LPTN model, a motor loss model has to be developed and it will be integrated with the thermal model. This loss model will be created in MATLAB/Simulink using a 3D scattered interpolation block that contains all the motor loss data set provided by the motor manufacturers or designers. Depending on the torque and speed conditions for UDDS and HWFET drive cycles, the loss model will determine dynamically appropriate losses. In this thesis, only constant torque–speed operating points are used to validate the LPTN model. The authors would like to continue this work to develop an integrated motor loss model and thermal model for dynamic simulation to predict motor temperature.

### References

- [1] L. V. Iyer, “Investigation of permanent magnet synchronous machines for direct–drive and integrated charging applications in electric vehicles,” Ph.D. Dissertation, University of Windsor, 2016.

- [2] N. Hashemnia and B. Asaei, “Comparative study of using different electric motors in the electric vehicles,” *International Conference on Electrical Machines*, 2008.
- [3] Z. Zhang, G. Li, Z. Qian, Q. Ye *et al.*, “Research on effect of temperature on performance and temperature compensation of interior permanent magnet motor,” *IEEE 11th conference on Industrial Electronics and Applications (ICIEA)*, 2016.
- [4] A. Sarikhani and O. Mohammed, “Real–time demagnetization assessment of PM synchronous machine,” *20th International Conference on Electrical Machines*, 2012.
- [5] T. Huynh and M. Hsieh, “Performance analysis of permanent magnet motors for electric vehicles (EV) traction considering driving cycles,” *Energies* 2018, vol. 11
- [6] P. Zhang, Y. Du, T. Habetler, and B. Lu, “A survey of condition monitoring and protection methods for medium voltage induction motors,” *IEEE Energy Conversion Congress and Exp.*, Nov. 2009.
- [7] P. Zhang, Y. Du, and T. Habetler, “A transfer–function–based thermal model reduction study for induction machine thermal overload protective relays,” *IEEE Transactions on Industry Applications*, vol. 46, no. 5, 2010.
- [8] F. Ahmed and N. C. Kar, “Analysis of end–winding thermal effects in a totally enclosed fan cooled induction motor with die cast copper rotor,” *IEEE Transactions on Industry Applications*, vol. 53, no. 3, pp. 3098–3109, 2017.
- [9] D. Staton and A. Cavagnino, “Convection heat transfer and flow calculations suitable for electric machines thermal models,” *IEEE Transactions on Industrial Electronics*, vol. 55, no. 10, pp. 3509–3516, Oct. 2008.
- [10] T. Huynh and M. Hsieh, “Comparative study of PM–assisted SynRM and IPMSM on constant power speed range for EV applications,” *IEEE Transactions on Magnetics*, vol. 53, no. 11, Nov. 2017.
- [11] S. Cash, Q. Zhou, O. Olatunbosun, H. Xu *et al.*, “New traction motor sizing strategy for an HEV/EV based on an overcurrent–tolerant prediction model,” *IET Intelligent Transport Systems*, vol. 13, no. 1, pp. 168–174, 2019
- [12] R. Tallam, S. Lee, G. Stone, G. Kliman *et al.*, “A survey of methods for detection of stator–related faults in induction machines,” *IEEE Transactions on Industry Applications*, vol. 43, no. 4, July/August 2007.

- [13] A. Acquaviva, O. Wallmark, E. Grunditz, S. Lundmark *et al.*, “Computationally efficient modeling of electrical machines with cooling jacket,” *IEEE Transactions on Transportation Electrification*, vol. 5, no. 3, 2019.
- [14] F. Ahmed, E. Ghosh, and N. C. Kar, “Transient thermal analysis of a copper rotor induction motor using a lumped parameter temperature network model,” *IEEE Transportation Electrification Conference and Expo (ITEC)*, June 2016.
- [15] J. Holman, *Heat Transfer*. 9th ed., McGraw–Hill, 2002, pp. 640–647.
- [16] J. Pyrhonen, T. Jokinen, and V. Hrabovcova, *Design of rotating electrical machines*. John Wiley & Sons, Ltd. 2008, ISBN: 978–0–470–69516–6.
- [17] F. Ahmed, P. Roy, M. Towhidi, G. Feng *et al.*, “CFD and LPTN hybrid technique to determine convection coefficient in end–winding of TEFC induction motor with copper rotor,” *IEEE 45th Annual Conference of Industrial Electronics Society*, Portugal, October 2019.
- [18] E. Ghosh, F. Ahmed, A. Mollaeian, J. Tjong *et al.*, “Online parameter estimation and loss calculation using duplex neural–lumped parameter thermal network for faulty induction motor,” in *Proc. of the IEEE Conference on Electromagnetic Field Computation*, Florida, 2016.
- [19] F. Ahmed, E. Ghosh, and N. C. Kar, “Transient thermal analysis of a copper rotor induction motor using a lumped parameter temperature network model,” in *Proc. of the IEEE Transportation Electrification Conference*, Michigan, USA, 2016.
- [20] E. Ghosh, F. Ahmed, and N. C. Kar, “Temperature influenced online stator resistance estimation using an improved swarm intelligence technique for induction machine,” in *proc. of IEEE Transportation Electrification Conference and Expo*, 2015.
- [21] K. Hafiz, G. Nanda, and N. C. Kar, “Comparative performance analysis of aluminum rotor and copper rotor SEIG considering skin effect,” in *Proc. of the IEEE International Conference on Electrical Machines*, Portugal, September 2008.

## CHAPTER 4

# CFD AND LPTN HYBRID TECHNIQUE TO DETERMINE CONVECTION COEFFICIENT IN THE END-WINDING OF A TEFC INDUCTION MOTOR WITH COPPER ROTOR

### *4.1. Introduction*

The stator end-windings generally reach the highest temperature compared to any other parts in a TEFC induction motor electric motor while it is in operation [1]. Determination of cooling effects on the end-windings in an induction motor with TEFC design is complex due to turbulent nature of air circulation around the end-winding in the motor endcaps. In [2]–[3] the end-winding cooling effects were investigated using computational fluid dynamic modeling and thermal experimentation on ARIM. The findings established the fact that the fins and blades on the rotor end-rings of an ARIM enhance the cooling effects on the end-winding and results higher convection coefficient. The higher the convection coefficient in the end-winding region the greater heat dissipation from the end-winding to the motor frame and endcaps. In [4]–[6], a LPTN modeling was proposed to determine convection coefficient in the end-winding region and compared their results with more LPTN modeling developed by several authors as shown in Figure 4.1 which shows the correlation between convection coefficient and air velocity inside the motor endcap. The higher the air circulation in the end-region the greater the cooling effects. The correlation of the convection coefficient consists of natural and forced convection coefficient, which varies with the inside air velocity. The findings in [4]–[6] also determines air velocity in the end-winding region as a function of rotor speed and fanning factor of the fins or blades on the rotor end-rings. For ARIM the fanning factor was determined between 0.8 and 1 depending on the size of the wafers incorporated on the rotor end-rings. It was also stated that if there is no internal fan or the ends of rotor are smooth, the internal air velocity will be much less and end-winding fanning factor will be zero. Hence, such lacking of evidence for fanning factor is an open problem that creates an opportunity and necessity to determine and quantify the convection heat transfer coefficient in the end-region for a CRIM that does not have any fins or blades on its rotor end-rings. This cooling differences due to the differences in the rotor geometry directly affects an accurate stator winding temperature

prediction for CRIM that are becoming widely and commonly used electric motor in many industry applications including electric vehicles. In addition, different size of the CRIM will experience different air circulation that has to be incorporated into this convection coefficient correlation.

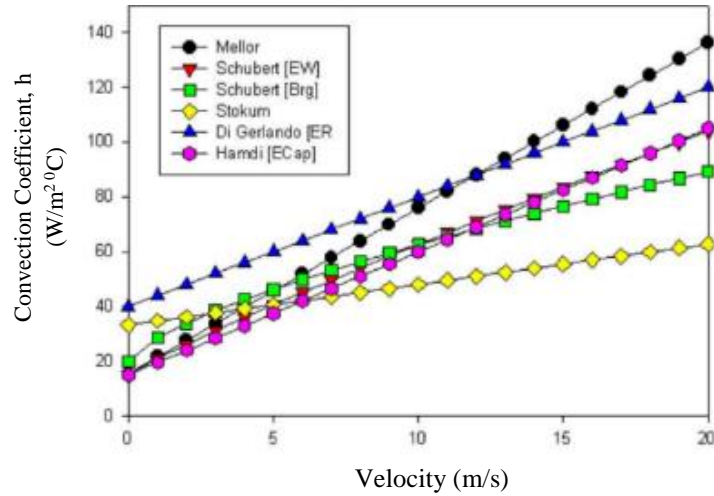


Figure 4.1. Published correlations for the equivalent heat-exchange coefficients in the end-regions for TEFC induction motors [3].

Hence, this chapter proposes a hybrid computational fluid dynamic and LPTN modeling techniques to determine effective air velocity inside motor endcap and its correlation with convection heat transfer coefficient for CRIM end-winding region. First, section II–A proposes a simplified LPTN modeling along with DC thermal tests on a 20 hp CRIM to determine the natural convection heat transfer coefficient. In order to determine forced convection heat transfer coefficient, it is required to determine air circulation and its velocity inside CRIM end-winding region. Section II–B proposes 2D and 3D computation fluid dynamic modeling to determine air circulation and air velocity magnitude that has been used for forced convection heat transfer coefficients in the end-winding region. Section III describes the experimental validation of the air circulation in the CRIM and proposes heat transfer modeling and implementation of empirical heat transfer relationships to determine convection heat transfer coefficients for CRIM or any other type of motors with different sizes that has smooth rotor ends.

## 4.2. Determination of Heat Transfer Coefficients

### 4.2.1. Natural Convection Coefficients from End-Winding

A simplified LPTN model in Figure 4.2 shows how the heat transfer takes place from the end-winding region to the motor casing. Heat from the stator winding in slots and end-winding flows through  $R_1$  and  $R_{eq}$  in parallel. Here,  $R_1$  means the equivalent thermal resistance between winding in slots and motor casing, and  $R_{eq}$  is the equivalent resistance between end-winding and motor casing. The details of  $R_{eq}$  is shown in detail in the right portion of the figure. Radiation heat transfer from the end-winding takes place through thermal resistance  $R_2$ , natural convection heat transfer takes place through thermal resistance  $R_3$  and forced convection heat transfer takes place through thermal resistance from end-winding to the inner air,  $R_4$  and then through resistance from inner air to the motor casing,  $R_5$ . In DC thermal tests, only copper losses at the stator exist which simplifies the calculation. As the rotor is still and does not have any rotation, thermal resistances,  $R_4$  and  $R_5$  for forced convection between the end-winding and the casing are cancelled out. During tests, temperatures at stator winding, inner air in the end-region and casing were measured using Resistance Temperature Detectors (RTDs) thermal sensors and these temperature readings are used in solving this LPTN to determine natural convection coefficients in the end-region of the motor. This natural convection takes place in the end-winding region only due to the non-existent of air circulation during DC tests. Figure 4.3 shows the temperature of the end-winding and inner air. The following sections describe the equations to calculate different thermal resistances from this simplified thermal model.

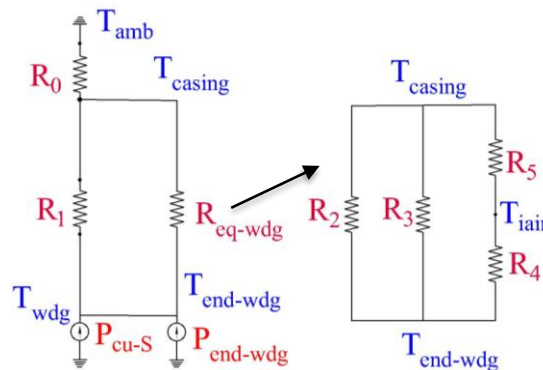


Figure 4.2. A simplified lumped parameter model for end-winding.



Table 4.1. Simplified Lumped Parameter Thermal Network Model

Item	Description of Model Parameters
$P_{cu-s}$	Stator copper losses (conductors in the slots)
$P_{end-wdg}$	Stator end-winding losses
$R_0$	Thermal resistance due to natural convection and radiation between casing and ambient
$R_1$	Equivalent thermal resistance due to conduction between stator winding in the slots and the motor casing
$R_2$	Thermal resistance due to radiation from end-winding to motor casing
$R_3$	Thermal resistance due to natural convection between end-winding to motor casing
$R_4$	Thermal resistance due to forced convection between end-winding and inner air
$R_5$	Thermal resistance due to forced convection between inner air to motor casing
$R_{eq}$	End-winding equivalent thermal resistance

Thermal resistance,  $R_0$  represents the resistance due to both natural convection and radiation between the casing and ambient air which can be calculated from the following expression:

$$R_0 = \frac{\Delta T_{casing}}{(P_{cu-s} + P_{end-wdg})} \quad (4.1)$$

Thermal resistance,  $R_1$  represents the resistance due to conduction between stator winding and the casing which can be calculated from the following expression:

$$R_1 = \frac{(T_{winding} - T_{casing})}{P_{cu-s}} \quad (4.2)$$

Thermal resistance,  $R_2$  represents the resistance due to radiation heat transfer between stator end-winding and the casing. Further,  $R_3$  represents the resistance due to natural convection between stator end-winding and the casing. Both resistances are connected in parallel and this can be calculated as:

$$\frac{1}{\left(\frac{1}{R_2} + \frac{1}{R_3}\right)} = \frac{(T_{winding} - T_{casing})}{P_{end-wdg}} \quad (4.3)$$

$$\frac{1}{R_2} = \sigma \epsilon A_{end-wdg} (T_{end-wdg} + T_{casing}) \times (T_{end-wdg}^2 + T_{casing}^2) \quad (4.4)$$

In order to calculate the convection coefficient due to natural convection from the end-winding (4.5) can be used:

$$R_3 = 1/h_{end-wdg}A_{end-cap} \quad (4.5)$$

where  $h_{end-wdg}$  is the convection heat transfer coefficient and  $A_{end-cap}$  is the endcap area. Table 4.2 shows equivalent circuit parameters for the test motor. Table 4.3 shows all the physical dimensions of the motor that are used in thermal resistance calculations. In estimating the stator end-winding copper losses and its impact on generating heat, it is important to know the length of the end windings with respect to the total of windings for each phase.

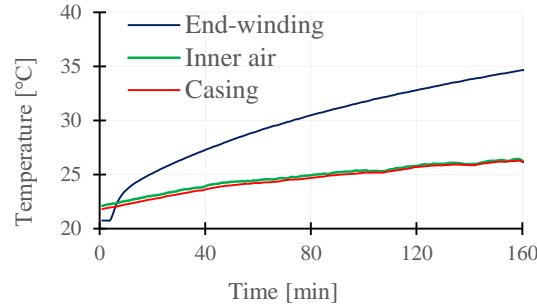


Figure 4.3. Measured temperatures for end-winding and inner air in the end-region.

The joule losses causing end windings heating will be proportional to the total joule losses caused by the whole length of the windings and is simplified as:

$$P_{end-wdg} = P_{cu-total} \times \left( L_{end-wdg} / L_S \right) \quad (4.6)$$

where  $L_{end-wdg}$  is the stator end-winding length,  $L_S$  is the total stator winding length. Table 4.4 shows all the calculated winding losses from DC tests and Table 4.5 shows the calculate results of the thermal resistances from the LPTN model. From these thermal resistances natural convection coefficient in the end-winding region was calculated using (4.5) which is the only convection coefficient as the rotor is not rotating during DC thermal tests. The following sections will determine the forced convection coefficients while the motor is driven at different speed conditions. First, Computational Fluid Dynamics (CFD) technique will be used to determine air flow characteristics and air velocity. Based on air flow pattern,

empirical relationships will be used to calculate forced convection coefficients.

Table 4.2. Copper Rotor Induction Test Motor Data

Test Motor Nameplate Data		Equivalent Circuit Parameters	
Parameter	Values	Parameter	Values (ohm)
Rated power	14.92 kW	$R_s$	0.36
Rated voltage	208/460 V	$R_R$	0.12
Rated current	50.0/25 A	$X_{ls}$	1.71
Rated speed	1,800 rpm	$X_{lr}$	1.71
Insulation class	F	$X_m$	28.20

Table 4.3. Key Physical Dimension Data of the Test Motor

Motor components	Values (meter)	Motor components	Values (meter)
Stator outer diameter	0.215	Shaft length (rotor)	0.228
Stator inner diameter	0.150	Shaft length from rotor end to the bearing	0.100
End-winding outer diameter	0.220		
End-winding inner diameter	0.190	Air thickness between rotor and endcap	0.036
End-winding axial length	0.070	Rotor yoke inner radius	0.098
Rotor length	0.228	Rotor yoke outer radius	0.107
Rotor outer diameter	0.154	Frame fin length	0.254
Shaft diameter	0.052	Frame fin width	0.007
Airgap length	0.0036	Rotor lamination thickness	0.0387
Frame length	0.315	Air thickness between rotor and endcap	0.036

Table 4.4. No Load Test Results for CRIM

Loading	$P_{cu-total}$ (Watt)	$L_{end-wdg}$ (m)	$L_S$ (m)	$P_{cu-S}$ (Watt)	$P_{end-wdg}$ (Watt)
No load	127	0.07	0.298	97	30

Table 4.5. No Load Test Results for CRIM

$R_0$ (°C/W)	$R_1$ (°C/W)	$R_2$ (°C/W)	$R_3$ (°C/W)	Equivalent of $R_2$ and $R_3$ (°C/W)	Natural Convection coefficient $h$ (W/m <sup>2</sup> .°C)
0.041	0.036	5.74	0.116	0.118	15.08

4.2.2. Determination of Air Flow Characteristics in the Stator End–Winding Region  
Using Computational Fluid Dynamic (CFD) Technique

i) Reynolds–averaged Navier–Stokes (RANS) Equations

CFD is used to determine air flow characteristics in the end–winding of the test motor. Navier–Stokes equations are the governing equations for a Newtonian fluid and dictate the conservation of mass, momentum and energy of the fluid element under consideration. The fluid is considered as a continuum so that the molecular structure and molecular motions of the fluid can be neglected and the analysis can be performed at macroscopic scale. For the CFD investigation of end–winding, Reynolds–averaged Navier–Stokes (RANS) equations are used in order to model the characteristics of the flow. The RANS model focuses on the mean flow and the effect of turbulence on the mean flow by time–averaging the Navier–Stokes equations. The continuity equation for the mean flow is

$$\frac{\partial U}{\partial x} + \frac{\partial V}{\partial y} + \frac{\partial W}{\partial z} = 0 \quad (4.7)$$

where  $\mathbf{U}$  is the mean velocity vector with components  $U$ ,  $V$  and  $W$  in  $x$ ,  $y$  and  $z$  directions, respectively. The rate of change of density has not been shown in the continuity equation because the inner air has been considered as an incompressible fluid. If the fluid were considered to be compressible, there would be one more term in the continuity equation for the rate of change of density. The momentum equations are

$$\frac{\partial U}{\partial t} + \text{div}(\mathbf{UU}) = -\frac{1}{\rho} \frac{\partial P}{\partial x} + \vartheta \text{div}(\text{grad } U) + \frac{1}{\rho} \left[ \frac{\partial(-\rho \overline{u^2})}{\partial x} + \frac{\partial(-\rho \overline{uv})}{\partial y} + \frac{\partial(-\rho \overline{uw})}{\partial z} \right] \quad (4.8)$$

$$\frac{\partial V}{\partial t} + \text{div}(\mathbf{VU}) = -\frac{1}{\rho} \frac{\partial P}{\partial y} + \vartheta \text{div}(\text{grad } V) + \frac{1}{\rho} \left[ \frac{\partial(-\rho \overline{uv})}{\partial x} + \frac{\partial(-\rho \overline{v^2})}{\partial y} + \frac{\partial(-\rho \overline{vw})}{\partial z} \right] \quad (4.9)$$

$$\frac{\partial W}{\partial t} + \text{div}(\mathbf{WU}) = -\frac{1}{\rho} \frac{\partial P}{\partial z} + \vartheta \text{div}(\text{grad } W) + \frac{1}{\rho} \left[ \frac{\partial(-\rho \overline{uw})}{\partial x} + \frac{\partial(-\rho \overline{vw})}{\partial y} + \frac{\partial(-\rho \overline{w^2})}{\partial z} \right] \quad (4.10)$$

where  $\mathbf{U}$  is the mean velocity vector with components  $U$ ,  $V$  and  $W$  in  $x$ ,  $y$  and  $z$  directions respectively,  $\mathbf{u}'$  is the velocity fluctuation vector with components  $u'$ ,  $v'$  and  $w'$  in  $x$ ,  $y$  and  $z$  directions respectively,  $P$  is the pressure of air,  $\vartheta$  is the kinematic viscosity of air. The

overbars indicate time-averaged quantities. The terms involving products of velocity fluctuation components in different directions are responsible for convective momentum transfer due to turbulent eddies. These can be thought of as additional turbulent stresses on the mean velocity components  $U$ ,  $V$  and  $W$  and are called Reynolds stresses. The Reynolds stresses ( $-\rho\overline{u_i' u_j'}$ ) are calculated by Boussinesq approximation

$$-\rho\overline{u_i' u_j'} = \mu_t \left( \frac{\partial U_i}{\partial x_j} + \frac{\partial U_j}{\partial x_i} \right) - \frac{2}{3} \rho k \delta_{ij} \quad (4.11)$$

where  $\rho$  is the density of air,  $\mu_t$  is the turbulent viscosity of air,  $U_i$  and  $U_j$  are mean velocity in  $i$  and  $j$  directions respectively,  $x_i$  and  $x_j$  indicate  $x$ ,  $y$  and  $z$  directions for  $i$  or  $j = 1, 2$ , and  $3$  respectively,  $k$  is the turbulent kinetic energy, the Kronecker delta  $\delta_{ij} = 1$  when  $i = j$  and  $\delta_{ij} = 0$  when  $i \neq j$ . The momentum equations dictate the conservation of momentum of fluid element.

The energy equation is

$$\begin{aligned} \frac{\partial E}{\partial t} + \text{div}(\mathbf{E}\mathbf{U}) = & \frac{1}{\rho} \text{div}(\Gamma \text{grad } T) + \tau_{xx} \frac{\partial U}{\partial x} + \tau_{yx} \frac{\partial U}{\partial y} + \tau_{zx} \frac{\partial U}{\partial z} + \tau_{xy} \frac{\partial V}{\partial x} + \tau_{yy} \frac{\partial V}{\partial y} + \\ & \tau_{zy} \frac{\partial V}{\partial z} + \tau_{xz} \frac{\partial W}{\partial x} + \tau_{yz} \frac{\partial W}{\partial y} + \tau_{zz} \frac{\partial W}{\partial z} \end{aligned} \quad (4.12)$$

where  $E$  is the energy,  $\Gamma$  is the effective thermal conductivity,  $T$  is the temperature,  $\tau_{ij}$  indicates the viscous stresses in the  $j$  direction on a surface normal to  $i$  direction.

The  $k$ - $\epsilon$  model is one of the turbulent models where two extra transport equations are used in addition to the continuity, momentum and energy equations to model the turbulent fluctuations. The transport equation for the turbulent kinetic energy is

$$\frac{\partial k}{\partial t} + \text{div}(k\mathbf{U}) = \frac{1}{\rho} \text{div} \left( \frac{\mu_t}{\sigma_k} \text{grad } k \right) + 2\vartheta_t S_{ij} \cdot S_{ij} - \epsilon \quad (4.13)$$

where  $k$  is the turbulent kinetic energy,  $\epsilon$  is the dissipation rate of turbulent kinetic energy,  $S_{ij}$  is the rate of deformation matrix in  $j$  direction on a surface normal to  $i$  direction, the subscripts indicate  $x$ ,  $y$  and  $z$  directions for  $i$  or  $j = 1, 2$  and  $3$  respectively,  $\mu_t = \rho C_\mu \frac{k^2}{\epsilon}$  is the eddy viscosity,  $\vartheta_t = \frac{\mu_t}{\rho}$  is the kinematic eddy viscosity, and the adjustable constants  $C_\mu = 0.09$ ,  $\sigma_k = 1$ . In (13),  $\frac{\partial k}{\partial t}$  is the rate of change of turbulent kinetic energy and  $\text{div}(k\mathbf{U})$  indicates the transport of turbulent convection. On the other hand, the transport of turbulent kinetic energy by diffusion is indicated by the divergence term on the right-hand side of

the equation. The term having turbulent viscosity and deformation matrix signifies the rate of production of turbulent kinetic energy. The last term with a negative sign means the destruction of turbulent kinetic energy.

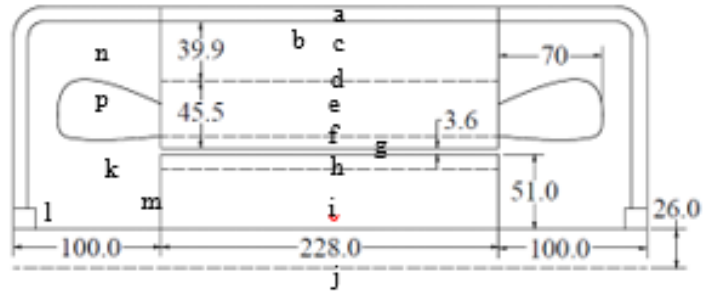
The transport equation for the rate of dissipation of turbulent kinetic energy is

$$\frac{\partial \varepsilon}{\partial t} + \text{div}(\varepsilon \mathbf{U}) = \frac{1}{\rho} \text{div} \left( \frac{\mu_t}{\sigma_\varepsilon} \text{grad } \varepsilon \right) + C_{1\varepsilon} \frac{\varepsilon}{k} 2\vartheta_t S_{ij} \cdot S_{ij} - C_{2\varepsilon} \frac{\varepsilon^2}{k} \quad (4.14)$$

where adjustable constants are  $\sigma_\varepsilon = 1.3$ ,  $C_{1\varepsilon} = 1.44$ , and  $C_{2\varepsilon} = 1.92$ . The first term on the left-hand side simply means the rate of change of  $\varepsilon$  and the second term indicates the transport of  $\varepsilon$  by convection. The divergence term on the right-hand side indicates the transport  $\varepsilon$  by diffusion. The term having turbulent viscosity and deformation matrix is the rate of production of  $\varepsilon$ , and it has a positive sign. The last term with a negative sign characterizes the rate of destruction of  $\varepsilon$  [12].

## ii) 2D and 3D End-Winding Model Setup

In the electric motor, two different domains are created in this exercise, one is rotating and the other is stationary. Multiple rotating reference frame technique in steady state analysis is used. The CRIM construction in Figure 4.4 shows all the major motor parts including end-winding which is considered in this study. The rotor geometry shows smooth rotor ends and no fins and blades on its end-rings. Figure 4.5 shows two 2D CFD models for the end-winding, one with completely smooth rotor ends and one with a small fin extension to demonstrate air circulations in the end-region. In both models, stator winding is created as solid body cross-section with 0% porosity. Rotor and shaft axis are identified as rotational axis and stator core, stator end-winding, casing, and endcap are considered as stationary walls. Fluid domain in different color represents a separate body from the winding, rotor, stator shaft, and casing walls. In the boundary condition, shaft axis and rotor axis were set as rotational reference at the speed of 1,200 and 200 r/min and stator and casing wall were set as stationary wall as shown in Figure 4.5.



- |                        |                 |                           |
|------------------------|-----------------|---------------------------|
| a. Motor frame         | f. Stator teeth | k. Air around end-winding |
| b. Stator yoke (upper) | g. Air-gap      | l. Bearing                |
| c. Stator core         | h. Rotor copper | m. Smooth rotor end       |
| d. Stator yoke (lower) | i. Rotor iron   | n. Non-ventilated         |
| e. Stator winding      | j. Shaft axis   | p. End-winding            |

Figure 4.4. CRIM construction for the proposed study.

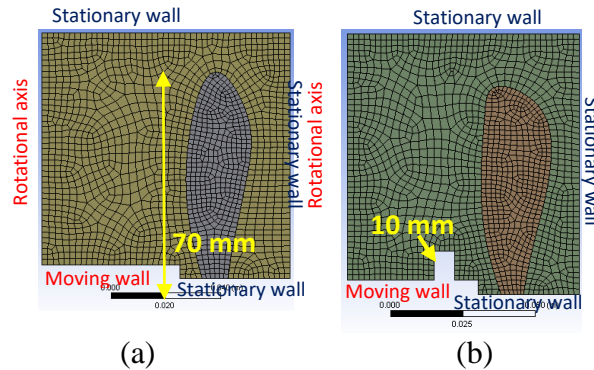


Figure 4.5. CFD models. (a) Smooth rotor end. (b) Small fin extensions.

Figure 4.6 shows a simplified 3D geometry of the rotor, shaft and air-gap region, excluding end-winding. The rotor and shaft were considered as a moving wall with a speed of 1,200 rpm and the fluid domain surface shown in the figure was considered as stationary wall because it is adjacent to stator inner diameter. For meshing, the element size was taken 5 mm and the element order was linear. No-slip condition was taken for both moving and stationary walls, because the air adjacent to the wall has the same velocity as the wall due to viscosity of air. Standard  $k-\epsilon$  model was used for the turbulence modeling with RANS equations in finite volume approach. The boundary conditions are shown in Table 4.6.

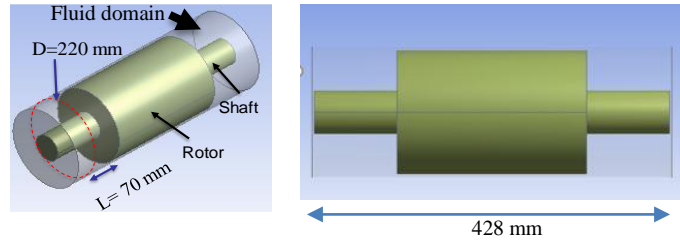


Figure 4.6. Simplified geometry. (a) Isometric view. (b) Side view.

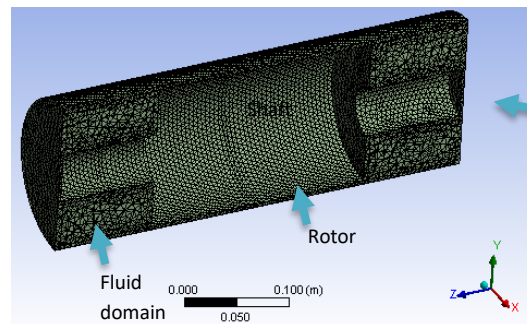


Figure 4.7. Mesh created for stator end-winding CFD model.

### iii) Results for 2D and 3D CFD Analysis

Steady state analysis was performed and from the simulation results, Figure 4.8 shows the air circulation in the end-winding region. Figure 4.8(a) shows the air velocity in the end-winding region to be in the range from 0.04 to 0.14 m/s for a rotor speed of 200 rpm. Figure 4.8(b) shows that the air velocity in the end-winding region is within the range from 0.15 to 0.51 m/s for a rotor speed of 1,200 rpm. In Figure 4.8(b), the air flow at 1200 r/min rotor speed spread more outward towards the motor endcap compared to that in Figure 4.8(a) at 200 r/min. There are two circulation loops produced in the region where the loop closer to the stator core has greater air circulation compared to the one close to the motor endcap. Velocity vector was used to better represent air circulation results for different speed settings. Considering physics, higher speed is creating stronger circulation compared to lower speed. Overall though, the air velocity magnitude is within the ranges from around 0.1 m/s to 0.5 m/s, which is not significant. This clearly demonstrates non-existent of rotor fins of blades like copper rotor creates weaker air velocity in the end-region.



Table 4.6. Boundary Conditions for 3D CFD Analysis

Component	Boundary conditions
Rotor and shaft	Wall motion: Moving wall (1200 rpm) Shear condition: No slip
Fluid Domain	Wall motion: Stationary wall Shear condition: No slip
Turbulence model	Standard k-epsilon
Mesh size	5 mm

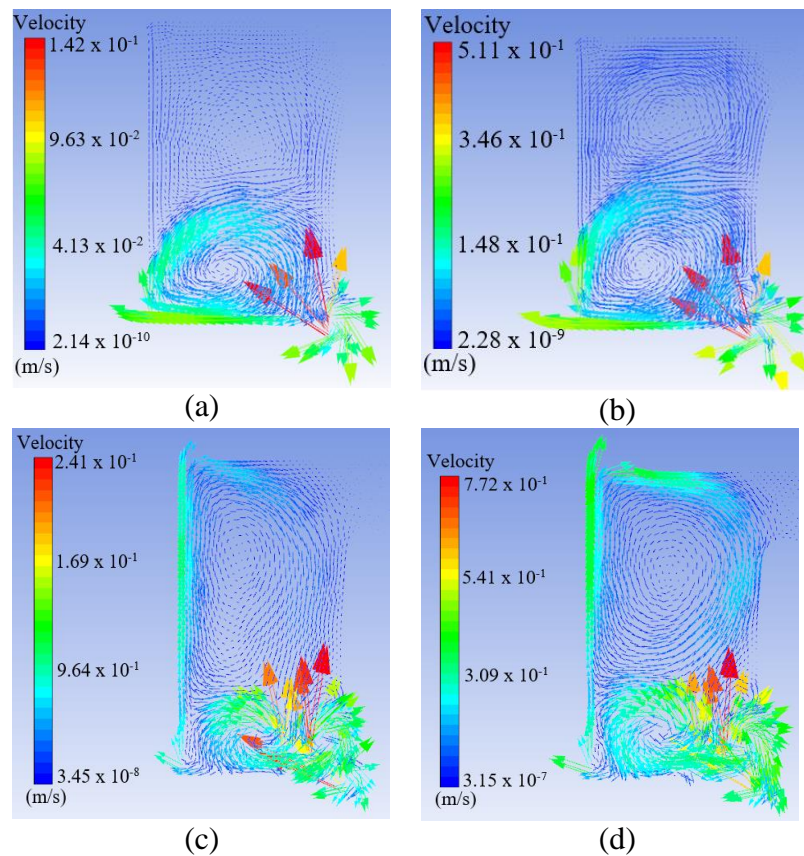


Figure 4.8. Air flow pattern in the end-winding. (a) At rotor speed 200 r/min and without fin. (b) At rotor speed 1,200 r/min and without fin. (c) At rotor speed 200 r/min and with fin. (d) At rotor speed 1,200 r/min and with fin.

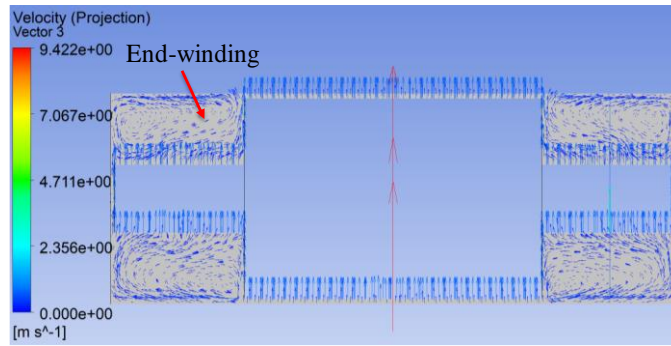


Figure 4.9. 3D CFD model simulated air velocity in the end-winding at 1,200 rpm (longitudinal section view).

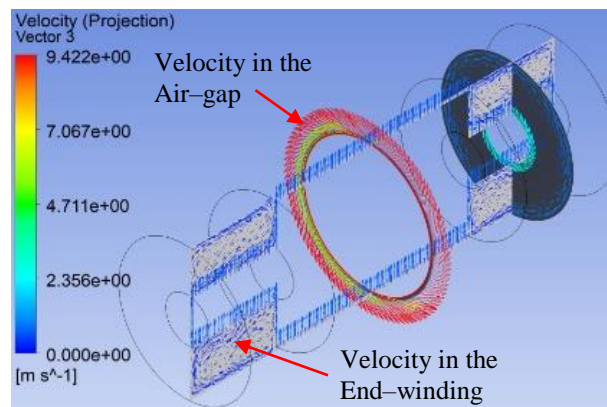


Figure 4.10. 3D CFD model simulated air velocity in the end-winding at 1200 rpm (isometric view).

The CFD model with a small fin extension that generates comparatively stronger air circulation as shown in Figures 4.8(c) and (d) that helps quicker heat dissipation through the endcap and casing. When the rotor speed is 200 rpm and a small fin is considered, the air velocity is in the range from 0.96 to 0.24 m/s, as shown in Figure 4.8(c). When the rotor speed is increased to 1200 rpm with the fin present, the air velocity remains within 0.31 to 0.77 m/s. The air velocity in the air-gap region has higher values in the outer surface adjacent to the stator and lower values in the inner surface adjacent to the rotor. The air velocity in the end-region has much lower value than in the air-gap region. Air velocity was further investigated using 3D CFD modeling where Figures 4.9 and 4.10 show that the air velocity in the air-gap achieves the highest value in the range of 5 m/s to 9 m/s and the air velocity in the end-winding region are in the range of 0.1 m/s to 0.6 m/s at 1200 r/min.

### 4.3. Validation of Air Flow Characteristics in the End-Winding Region through Experiments

In order to validate air flow characteristics in the end-region from CFD simulation study, experimentally air velocity was measured in the end-region. Figure 4.11 shows the experimental setup measuring air velocity while the test motor is driven at a speed of 1200 r/min, 600 r/min and 200 r/min. A hot wire anemometer was used to measure the velocity and the results are shown in Figures 4.12 and 4.13. The results show that air velocity is higher close to rotational axes of the rotor and the shaft. The velocity gets weaker as it moves towards the motor endcap.

The general equation to determine convection coefficient is expressed as (4.15):

$$h_{combined} = Nu \times k_{air} / d \quad (4.15)$$

where,  $h_{combined}$  is the combination of natural and forced convection coefficients,  $Nu$  is the Nusselt number,  $d$  is the diameter of the cylinder and  $k_{air}$  is the thermal conductivity. It is important to note that convection heat transfer coefficient is greatly influenced by the air velocity as well as flow characteristics whether it is laminar or turbulent [11]. From Computational Fluid Dynamics (CFD) analysis, it has been determined that flow pattern in the end-region of an electric motor even with smooth rotor ends such as Copper Rotor Induction Motor (CRIM) is turbulent in nature. Such air circulations indicate that the heat transfer in the end-winding region takes place due to forced convection.

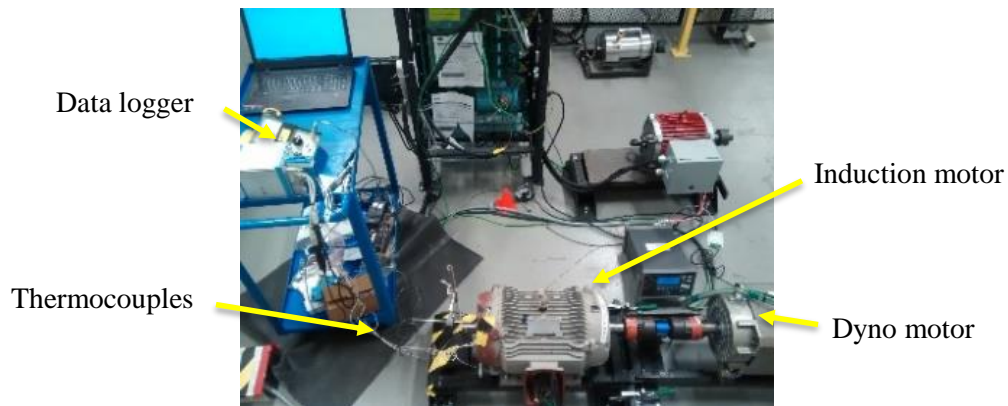


Figure 4.11. Experimental set-up for thermal tests on a 20hp CRIM.

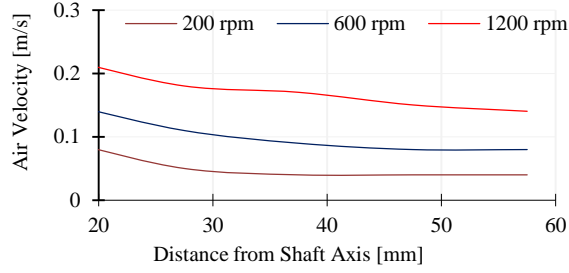


Figure 4.12. Measured air velocity in the vertical axis to the end-winding plane.

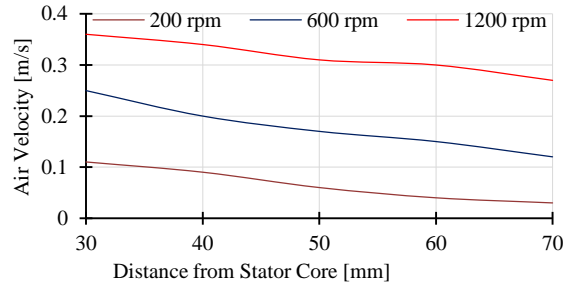


Figure 4.13. Measured air velocity in the horizontal axis to the end-winding plane.

On the other hand, for smooth rotor geometry, the circulation is not strong enough and air velocity ranges for the Copper Rotor Induction Motor (CRIM) motor 0.1 m/s to 0.5 m/s depending on the rotor speed ranges from 200 r/min to 1200 r/min. Hence, convection heat transfer will consist of both free convection and forced convection in the end-winding region.

The free convection boundary layer equation will indicate the general criterion for determining whether free convection effects dominate. The criterion for free convection dominance is expressed as:

$$\frac{Gr}{Re^2} > 10 \quad (4.16)$$

From Computational Fluid Dynamic (CFD) analysis in Figures 4.8, and 4.9, stronger air circulation exists primarily close to the stator core end. This space can be assumed as a cylinder that contains the circulation.

A relationship between  $Re$  and  $GrPrD/L$  was graphically shown in [11], where  $Re$  is Reynolds number,  $Gr$  is Grashof number,  $Pr$  is Prandtl number,  $D$  is the hydraulic diameter and  $L$  is the length of the cylinder in which the fluid circulation occurs. Empirical equations

for Nusselt number proposed by different researchers were shown to be applicable in different regions of the graph depending on the values of  $Re$  and  $GrPrD/L$ . Higher value of  $Re$  indicates turbulent nature of the flow, whereas lower  $Re$  value indicates laminar nature. On the other hand, higher value  $GrPrD/L$  indicates more forced convection and lower value indicates natural convection. Sieder and Tate's equation was applicable for forced convection in laminar flow; Oliver's equation was applicable for mixed convection in laminar flow; Metais's equation was applicable for mixed convection in turbulent flow; and Hausen's equation was found suitable for forced convection in turbulent flow. The value of Reynold number becomes  $1.35 \times 10^3$  at a speed of 200 r/min and  $5.51 \times 10^3$  at a speed of 1200 r/min. This range of Reynolds number indicates that combined convection takes place in the end-winding region as well as the flow is turbulent in nature. Thus, the following empirical equation for mixed convection for turbulent flow proposed by Metais can be used to calculate the Nusselt number which is the key parameter to calculate combined convection coefficient [11].

$$Nu = 4.69 \times Re^{0.27} \times Pr^{0.21} \times Gr^{0.07} \times \left(\frac{d}{L}\right)^{0.36} \quad (4.17)$$

where,  $Nu$  is the Nusselt number,  $Re$  is the Reynolds number,  $Pr$  is the Prandlt number,  $Gr$  is the Grashof number,  $d$  is the average diameter of stator end-winding and  $L$  is the axial length of end-winding. Reynolds number is defined as the ratio of inertia force to viscous force acting on a fluid flow. It is determined as follows

$$Re = \frac{\rho \times v_{air} \times d}{\mu} \quad (4.18)$$

where  $\rho$  is the density of air,  $v_{air}$  is the air velocity and  $\mu$  is the dynamic viscosity of air.

Prandtl number is defined as the ratio of momentum diffusivity to thermal diffusivity of the fluid, and it is determined as follows

$$Pr = \frac{\mu \times c_p}{k} \quad (4.19)$$

where  $c_p$  is the specific heat capacity of air and  $k$  is the thermal conductivity of air.

Grashof number is the ratio of buoyancy force to viscous force acting on a fluid, and it is found from the following equation.

$$Gr = \frac{\rho^2 \times g \times \beta \times (T_{end-wdg} - T_{air}) \times d^3}{\mu^2} \quad (4.20)$$

where  $g$  is the gravity,  $\beta$  is the reciprocal of inner air  $T_{air}$  and  $T_{end-wdg}$  is the end-winding temperature.

From the mathematical solution using equations (4.17)–(4.20), Nusselt number was calculated and combined convection coefficient was calculated from (15). Steady state temperatures of  $T_{air}$  and  $T_{end-wdg}$  were measured from no load experiments on the CRIM test motor. Table 4.7 shows calculated results of Nusselt number and convection coefficients for different air velocity. The value of  $Gr/Re^2$  is also tabulated in the Table 4.7, which is the indication of the existence of natural convection and forced heat transfer in the end-winding region of the CRIM test motor.

Combined convection coefficient results are plotted related to rotor peripheral speed as shown in Figure 4.14. The equations for graphs are displayed. If the line in the graph is extended towards left, it will intersect the y-axis ( $h_{combined}$ ) at a value of  $13.633 \text{ W/m}^2 \cdot ^\circ\text{C}$  and the rotor speed or peripheral rotor speed is zero. This clearly determines that the combined convection coefficient is:

$$h_{combined} = 0.4072 a r_p + b \quad 13.633 \quad (4.21)$$

where  $a = 0.4072 \text{ J/m}^3 \cdot ^\circ\text{C}$ ,  $r_p$  is the rotor peripheral speed in m/s, and  $b = 13.633 \text{ W/m}^2 \cdot ^\circ\text{C}$ .

Table 4.7. Combined Natural and Forced Convection Heat Transfer Coefficients at Different Rotor RPM

Rotor RPM	Inner air velocity, $V_{air}$ (m/s)	Nusselt Number (Nu)	Combined Convection coefficient ( $\text{W/m}^2 \cdot ^\circ\text{C}$ )	$Gr/Re^2$
200	0.1	123.56	14.97	0.040
600	0.2	147.26	17.49	0.13
1200	0.4	178.68	21.48	0.79

where,  $h_{combined}$  is the combined convection coefficient, complete natural convection coefficient is  $13.633 \text{ W/m}^2\cdot\text{°C}$  and forced convection coefficient is  $0.4072r_p$ . Forced convection coefficient is a function of rotor peripheral speed of  $r_p$ . This combined convection coefficient is compared with the findings from the past researchers which is shown in Figure 4.15. The comparison in Figure 4.15 clearly determines the differences in the values of natural and forced convection coefficients between the published and the one calculated in this work. This difference is caused due to the rotor geometry with or without fins on its end-rings. In Figure 4.15, all the published ones are convection coefficients for induction motor with aluminum rotor that has fins on its rotor end rings and  $h_{combined}$  found in this paper for CRIM that has smooth rotor ends. It is critical to note that both natural and forced convection coefficients for CRIM have lower values compared to aluminum rotor induction motor as expected due to smooth rotor end of CRIM.

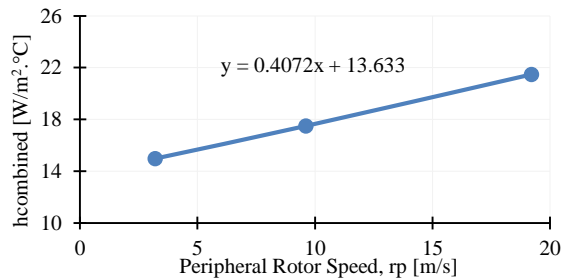


Figure 4.14. Combined convection coefficient with rotor peripheral speed (m/s).

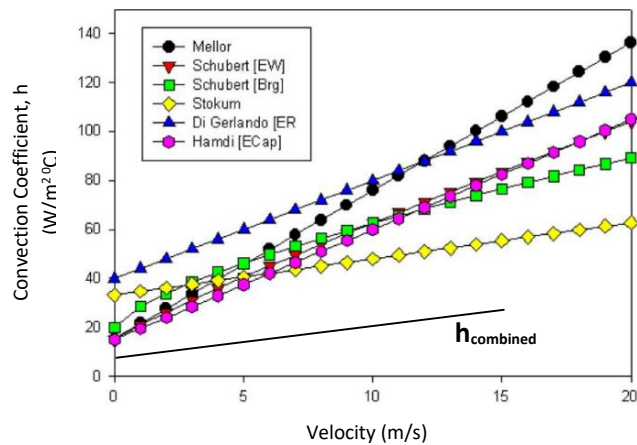


Figure 4.15. Comparison of proposed correlation for convection coefficient with the published ones by other models.

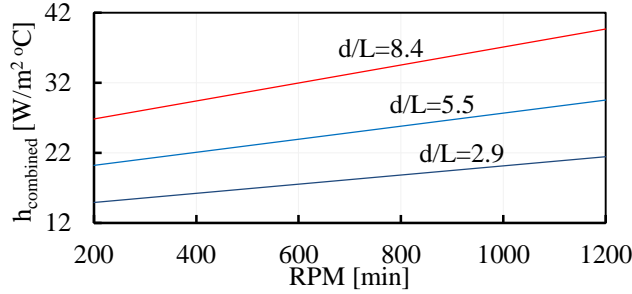


Figure 4.16. Convection coefficient in the end-winding of the motor that has no fins on its end-rings.

It is also important to note that the natural convection coefficient component from (4.21) which is  $13.633 \text{ W/m}^2\text{°C}$  compares very close to the value of the natural convection coefficient of  $15.08 \text{ W/m}^2\text{°C}$  in Table 4.3 that was determined from the proposed LPTN model solution technique. This comparison further confirms that the combined convection coefficient  $h_{combined}$  found for CRIM is accurate enough to be used in stator winding temperature prediction. In order to calculate convection coefficient in the end-winding for any size of the motor, the relationship between motor speed and combined convection coefficient has been determined based on the findings in this work as shown in the Figure 4.16. From this relationship, the convection coefficient can be found with respect to speed of the motor and  $d/L$  ratio, where  $d$  is the average diameter of the end-winding and  $L$  is the axial length of the end-winding. For the prototype test motor that is used in this research,  $d = 205 \text{ mm}$  and  $L = 70$ , so  $d/L = 2.9$ . As a result, the convection coefficient  $h_{combined} = 22 \text{ W/m}^2\text{°C}$  at 1,200 rpm.

#### 4.4. Conclusion

In this chapter, a simplified LPTN and CFD hybrid technique has been proposed to determine the end-winding convection coefficient. This is a critical thermal parameter to accurately predict stator winding temperature to ensure proper overload thermal protection for an electric motor that has smooth rotor geometry such as CRIM. The key objectives that are met in this work are as follows:

- Natural convection coefficient in the end-winding was found using a simplified LPTN model and DC thermal tests.
- Air flow characteristics in the end-winding region have been determined.
- Combined natural and forced convection coefficient for end-winding has been found



by analytical solution using empirical heat transfer equations and air flow characteristics from 2D and 3D CFD simulations.

- A novel relationship between end-winding convection coefficient and motor rpm has been found and it is applicable to any size of copper rotor induction motor.
- The final finding of the chapter is that the convection coefficient in the end-winding region can be found for any size of copper rotor induction motor by using the corresponding diameter to length ration in the proposed equations.

Hence, these findings of convection coefficient in the end-winding region for CRIM that has smooth rotor ends is critically important to determine the stator winding temperature accurately for motor thermal protection.

### **References**

- [1] F. Ahmed and N. C. Kar, "Analysis of end-winding thermal effects in a totally enclosed fan cooled induction motor with die cast copper rotor," *IEEE Transactions on Industry Applications*, vol. 53, no. 3, pp. 3098–3109, 2017.
- [2] C. Micallef, S. J. Pickering, K. Simmons, and K. Bradley, "Improvements in air flow in the end region of a large totally enclosed fan cooled induction motor," *IEEE International Electric Machines and Drives Conference*, San Antonio, May 2005.
- [3] C. Micallef, S. J. Pickering, K. A. Simmons, and K. J. Bradley, "An alternative cooling arrangement for the end region of a totally enclosed fan cooled (TEFC) induction motor," *4th IET Conference on Power Electronics Machines and Drives*, 2008, pp. 309–309.
- [4] A. Boglietti and A. Cavagnino, "Analysis of the end-winding cooling effects in TEFC induction motors," *IEEE Transactions on Industry Applications*, vol. 43, no. 5, pp. 1214–1222, 2007.
- [5] A. Boglietti, A. Cavagnino, D. Staton, M. Popescu, C. Cossar, and M. I. McGilp, "End space heat transfer coefficient determination for different induction motor enclosure types", *IEEE Trans. on Industry Applications*, vol. 45, no. 3, pp. 929–937, May/June 2009.
- [6] A. Boglietti, A. Cavagnino, D. Staton, and M. Popescu, "Impact of different end region cooling arrangements on end-winding heat transfer coefficients in electric motors," in *Proc. IEEE Conf., on Industrial Electronics*, 2009.

- [7] A. Boglietti, A. Cavagnino, M. Lazzari, and M. Pastorelli, "A simplified thermal model for variable speed self cooled industrial induction motor," *IEEE Transactions on Industry Applications*, vol. 39, no. 4, pp. 945–952, July/August 2003.
- [8] E. Schubert, "Heat transfer coefficients at end windings and bearing covers of enclosed asynchronous machines," *Elektrie*, vol. 22, pp. 160-162 (Translation ERA/IB 2846), April. 1968.
- [9] D. A. Staton and A. Cavagnino, "Convection heat transfer and flow calculations suitable for electric machines thermal models," *IEEE Transactions on Industrial Electronics*, vol. 55, no. 10, Oct. 2008.
- [10] F. Ahmed, E. Ghosh, and N. C. Kar, "Transient thermal analysis of a copper rotor induction motor using a lumped parameter temperature network model," in *IEEE Transportation Electrification Conference and Expo (ITEC)*, June 2016.
- [11] J. P. Holman, *Heat transfer*. 9<sup>th</sup> ed., New York: McGraw–Hill, 2002, pp. 640–647.
- [12] H. K. Versteeg and W. Malalasekera, *An introduction to computational fluid dynamics–The finite volume approach*, 2nd ed., Pearson Education Limited, Harlow, England, 2007, pp. 72–76.
- [13] J. Pyrhonen, T. Jokinen, and V. Hrabovcova, *Design of rotating electrical machines*. John Wiley & Sons Ltd, 2008, ISBN: 978–0–470–69516–6.
- [14] E. Ghosh, F. Ahmed, A. Mollaeian, and N. C. Kar, "Online parameter estimation and loss calculation using duplex neural–lumped parameter thermal network for faulty induction motor," in *Proc. Of the IEEE Conference on Electromagnetic Field Computation*, Florida, 2016.
- [15] F. Ahmed, E. Ghosh, and N. C. Kar, "Transient thermal analysis of a copper rotor induction motor using a lumped parameter temperature network model," in *Proc. Of the IEEE Transportation Electrification Conference*, Michigan, USA, 2016.
- [16] E. Ghosh, F. Ahmed, and N. C. Kar, "Temperature influenced online stator resistance estimation using an improved swarm intelligence technique for induction machine," in *Proc. of IEEE Transportation Electrification Conference and Expo*, 2015.
- [17] M. Hossain, R. Fdhila, and K. Ronnberg, "Taylor–Couette flow and transient heat transfer inside the annulus air–gap of rotating electrical machines," *Applied Energy*, vol. 207, December 2017, pp. 624–633.

- [18] A. Tovar–Barranco, A. Lopez–de–Heredia, I. Villar, and F. Briz, “Modeling of end–space convection heat–transfer for internal and external rotor PMSMs with fractional–slot concentrated windings,” *IEEE Transactions on Industrial Electronics*, 2020.
- [19] P. Pescetto, S. Ferrari, G. Pellegrino, E. Carpaneto, and A. Boglietti, “Winding thermal modeling and parameters identification for multi–three phase machines based on short–time transient tests,” *IEEE Transactions on Industrial Electronics*, 2020.
- [20] T. Dong, X. Zhang, F. Zhou, and B. Zhao, “Correction of winding peak temperature detection in high–frequency automotive electric machines,” *IEEE Transactions on Industrial Electronics*, vol. 67, no. 7, 2020.
- [21] S. Rocca, S. Pickering, C. Eastwick, C. Gerada, and K. Ronnberg, “Numerical study on the impact of end windings porosity on the fluid flow and heat transfer in a totally enclosed fan–cooled electrical machine,” *IEEE International Electric Machines & Drives Conference (IEMDC)*, 2019.
- [22] D. Liang, Z. Zhu, J. Feng *et al.*, “Influence of critical parameters in lumped–parameter thermal models for electrical machines,” *22<sup>nd</sup> International Conference on Electrical Machines and Systems*, 2019.
- [23] D. Camilleri, A. Bell, R. Rolston, and A. Kakade, “An experimental and numerical study of airflow behaviour in a low–voltage concentric–wound machine,” *IEEE Workshop on Electrical Machines Design, Control and Diagnosis*, 2017.
- [24] S. Nategh, Z. Huang, A. Krings *et al.*, “Thermal modeling of directly cooled electric machines using lumped parameter and limited CFD analysis,” *IEEE Transactions on Energy Conversion*, 2013.
- [25] A. Acquaviva, O. Wallmark, E. Grunditz *et al.*, “Computationally efficient modeling of electrical machines with cooling jacket,” *IEEE Transactions on Transportation Electrification*, vol. 5, no. 3, 2019.

## **CHAPTER 5**

### **CONCLUSION AND FUTURE WORK**

#### ***5.1. Conclusion***

This thesis proposed LPTN thermal modeling that can dynamically predict the motor temperature by providing optimum liquid cooling requirements.

Chapter 1 was an introduction to the research topic and discussed why this research is important and relevant to the industry applications. It clearly states the objectives and explained the novelty of this research work.

Chapter 2 was a review study of thermal modeling for traction motors. LPTN model was found to be more efficient for thermal analysis of electric motors in electric vehicle applications. It was recommended that LPTN modeling must include complete heat dynamics that take place in all the major motor parts while it is operation in order to predict motor temperature accurately.

A simplified LPTN modeling with liquid cooling was proposed in Chapter 3 to predict motor temperature under different vehicle driving conditions. The required amount of heat removal from the motor was determined from the LPTN in order to keep the motor temperature within the safe limit under varying motor driving conditions. The LPTN model was developed and created using MATLAB Simulink software. A carefully designed cooling block was implemented in the LPTN modeling in order to be able to regulate the required flow rate of the coolant. The findings that are found in this research work can be potentially used in electric vehicles to predict dynamically motor temperature by providing adequate liquid cooling. An optimum coolant flow rate was determined from the proposed heat transfer solution in LPTN modeling, which will eventually lead to further development of a motor protection algorithm in an electric vehicle.

A hybrid technique of LPTN modeling and CFD analysis for determining end-winding convection coefficient was demonstrated in Chapter 4. A novel mathematical relationship was established between rotor speed and convection coefficients in the end-winding region. This relationship will be used for determining the convection coefficient in the

motors that has smooth rotor ends and until now estimation of end-winding convection coefficient is an open problem in LPTN thermal model analysis to predict motor temperature accurately.

### ***5.2. Future Work***

The proposed LPTN model with liquid cooling design can be implemented in the software program for dynamic temperature prediction under different EV drive cycles. It can be an algorithm for motor thermal protection in dynamic conditions. As the required flow rate is determined from the predicted temperature, the cooling effect will be adequate to keep the motor within the safe temperature limit. This will help in predicting motor thermal health for different EV drive cycles satisfying longer driving ranges.

The future work as a continuation of this research will be as follows:

1. Dynamic motor temperature prediction tool will be developed for a full-scale IPMSM prototype by coupling the LPTN thermal modeling with an electromagnetic motor model.
2. Optimum cooling solution will be determined from the proposed LPTN model with a full-scale IPMSM.
3. Mechanical optimization of cooling channel design will be performed using CFD techniques.
4. Experiments will be conducted on a full-scale motor with active liquid cooling in the CHARGE lab to validate the proposed LPTN model.
5. The LPTN modeling will further be extended and modified for online temperature prediction of different types of traction motors designed and prototyped in the CHARGE lab.

## APPENDIX

Permissions for using the previously published works are given below:



Home Help Email Support Muhammad Towhidi

### A Comprehensive Review of Thermal Design and Analysis of Traction Motors



Requesting permission to reuse content from an IEEE publication

**Conference Proceedings:**  
2019 IEEE 28th International Symposium on Industrial Electronics (ISIE)

**Author:**  
Pratik Roy; Muhammad Towhidi; Firoz Ahmed; Alexandre J. Bourgault; Shruthi Mukandar; Aiswarya Balamurali; Narayan C. Kar

**Publisher:** IEEE

**Date:** 12-14 June 2019

*Copyright © 2019, IEEE*

### Thesis / Dissertation Reuse

The IEEE does not require individuals working on a thesis to obtain a formal reuse license, however, you may print out this statement to be used as a permission grant:

*Requirements to be followed when using any portion (e.g., figure, graph, table, or textual material) of an IEEE copyrighted paper in a thesis:*

- 1) In the case of textual material (e.g., using short quotes or referring to the work within these papers) users must give full credit to the original source (author, paper, publication) followed by the IEEE copyright line © 2011 IEEE.
- 2) In the case of illustrations or tabular material, we require that the copyright line © [Year of original publication] IEEE appear prominently with each reprinted figure and/or table.
- 3) If a substantial portion of the original paper is to be used, and if you are not the senior author, also obtain the senior author's approval.

*Requirements to be followed when using an entire IEEE copyrighted paper in a thesis:*

- 1) The following IEEE copyright/ credit notice should be placed prominently in the references: © [year of original publication] IEEE. Reprinted, with permission, from [author names, paper title, IEEE publication title, and month/year of publication]
- 2) Only the accepted version of an IEEE copyrighted paper can be used when posting the paper or your thesis online.
- 3) In placing the thesis on the author's university website, please display the following message in a prominent place on the website: In reference to IEEE copyrighted material which is used with permission in this thesis, the IEEE does not endorse any of [university/educational entity's name goes here]'s products or services. Internal or personal use of this material is permitted. If interested in reprinting/republishing IEEE copyrighted material for advertising or promotional purposes or for creating new collective works for resale or redistribution, please go to [http://www.ieee.org/publications\\_standards/publications/rights/rights\\_link.html](http://www.ieee.org/publications_standards/publications/rights/rights_link.html) to learn how to obtain a License from RightsLink.

If applicable, University Microfilms and/or ProQuest Library, or the Archives of Canada may supply single copies of the dissertation.

BACK CLOSE WINDOW

**20PFL-0972/2020-01-0455 - Lumped Parameter Thermal Network Modeling for Online Temperature Prediction of Permanent Magnet Synchronous Motor for Different Drive Cycles in Electric Vehicle Applications**

- [Copyright assignment completed.](#)

Copyright Assignment		
Muhammad Towhid		
	Copyright Type	Copyright Assignment Date
Muhammad Towhid	SAE	Jan 28, 2020
Narayan C. Kar		
Shruthi Mukundan		
Ze Li		
Firoz Ahmed		

**Selected copyright info**

("Work"). Assignor hereby assigns to SAE all rights, titles and interest in and to Assignor's copyright in the Work in the exclusive rights. If the Work is a work-made-for-hire pursuant to 17 USC § 101 of the Copyright Act, then such undersigned entity (e.g., employer, consortium, sponsoring entity) shall be deemed the Author for purposes of this Assignment and is the only recognized entity able to assign copyright. All works, image and text, created for an entity as part of a contracted position may be considered third party content. If said content is incorporated in the aforementioned Work, it is the responsibility of the author(s) to certify and carryout the requirements for acquiring republishing permission prior to submitting for publication, and the authors are required to include the appropriate licensing release documentation with the final Work.

Assignor represents, warrants and guarantees that (1) the Work is an original unpublished work; (2) Assignor is the sole and exclusive owner and claimant of all rights, titles and interest in and to the Work, including all copyrights therein, no other party, including an employer or contract provider may claim ownership to the Work's attributed copyrights, and neither the Work nor copyrights have been assigned, transferred or otherwise encumbered; (3) the Work contains no material which would violate any copyright or other personal or proprietary right of any person or entity if published; (4) the Work is not a work made for the United States Government or a foreign government; and (5) Assignor has the authority to transfer the rights to SAE and cause this Assignment to be executed as of the date first written above. Assignor further represents, warrants and guarantees to indemnify SAE in the event a claim is made of copyright ownership for the Work or a portion thereof.

Assignor further represents, warrants and guarantees, to the best of Assignor's knowledge and ability, that the Work is NOT controlled for export from the United States to any non-U.S. person or any other nation under the International Traffic in Arms Regulations (22 CFR Parts 120-130) or the Export Administration Regulations (15 CFR Parts 730-774) and, accordingly, may be modified, used, copied, distributed or circulated by SAE, in whole or in part, without any export licenses under the foregoing regulations.

Assignor agrees that it shall not dispute, contest, aid or assist others in disputing or contesting, either directly or indirectly, SAE's exclusive rights, titles and interest in the Work and in any and all compilations, customizations, collective works and/or derivative works based on the Work, including copyrights therein or other proprietary rights therein claimed by SAE.

Assignor agrees that, for no additional compensation, Assignor will execute any and all documents that may be necessary to assist SAE to register, protect and enforce SAE's rights in and to the Work and any and all compilations, customizations, collective works and derivative works based on the Work.

SAE hereby grants Assignor the nonexclusive right to reproduce and distribute the Work (including tables, graphs or other figures therein) in print and electronic format following six (6) months after first publication by SAE. Assignor may reproduce and distribute the Work for non-commercial purposes only, and the Work shall not be offered for sale or used to imply endorsement by SAE of a service or product. Notwithstanding the foregoing, Assignor may reproduce and distribute Assignor-authored individual tables, graphs or other figures included in the Work, in additional Assignor-authored publications, for commercial purposes. Any reproduction or distribution of the Work (including tables, graphs or other figures therein) must acknowledge SAE as original publisher and include the names of all author(s), the publication title, and an appropriate copyright notice that identifies SAE as the copyright holder. The Assignor may also post an electronic version of the accepted Work to an institutional repository, but not the final, typeset Work. The final, typeset, published version of the Work may not be posted online in any manner to accommodate free public access without prior written approval by SAE.





### CFD and LPTN Hybrid Technique to Determine Convection Coefficient in End-winding of TEFC Induction Motor with Copper Rotor

Conference Proceedings:

IECON 2019 - 45th Annual Conference of the IEEE Industrial Electronics Society

Author: Firoz Ahmed

Publisher: IEEE

Date: Oct. 2019

Copyright © 2019, IEEE

#### Thesis / Dissertation Reuse

The IEEE does not require individuals working on a thesis to obtain a formal reuse license, however, you may print out this statement to be used as a permission grant:

*Requirements to be followed when using any portion (e.g., figure, graph, table, or textual material) of an IEEE copyrighted paper in a thesis:*

- 1) In the case of textual material (e.g., using short quotes or referring to the work within these papers) users must give full credit to the original source (author, paper, publication) followed by the IEEE copyright line © 2011 IEEE.
- 2) In the case of illustrations or tabular material, we require that the copyright line © [Year of original publication] IEEE appear prominently with each reprinted figure and/or table.
- 3) If a substantial portion of the original paper is to be used, and if you are not the senior author, also obtain the senior author's approval.

*Requirements to be followed when using an entire IEEE copyrighted paper in a thesis:*

- 1) The following IEEE copyright/ credit notice should be placed prominently in the references: © [year of original publication] IEEE. Reprinted, with permission, from [author names, paper title, IEEE publication title, and month/year of publication]
- 2) Only the accepted version of an IEEE copyrighted paper can be used when posting the paper or your thesis online.
- 3) In placing the thesis on the author's university website, please display the following message in a prominent place on the website: In reference to IEEE copyrighted material which is used with permission in this thesis, the IEEE does not endorse any of [university/educational entity's name goes here]'s products or services. Internal or personal use of this material is permitted. If interested in reprinting/republishing IEEE copyrighted material for advertising or promotional purposes or for creating new collective works for resale or redistribution, please go to [http://www.ieee.org/publications\\_standards/publications/rights/rights\\_link.html](http://www.ieee.org/publications_standards/publications/rights/rights_link.html) to learn how to obtain a License from RightsLink.

If applicable, University Microfilms and/or ProQuest Library, or the Archives of Canada may supply single copies of the dissertation.

BACK

CLOSE WINDOW

## VITA AUCTORIS

NAME: Muhammad Ali Ayub Towhidi

PLACE OF BIRTH: Rajshahi, Bangladesh

YEAR OF BIRTH: 1994

EDUCATION: Govt. Laboratory High School, Rajshahi,  
Bangladesh, 2010

Rajshahi College, Rajshahi, Bangladesh, 2012

Bangladesh University of Engineering and  
Technology, B.Sc., Dhaka, Bangladesh, 2017